UCRL-ID-131775

Fracture/Matrix Flow Experiments Results

D. Wildenschild
M.S. Costantino
J.J. Roberts
T.J. Kneafsey
W. Lin

September 30, 1998

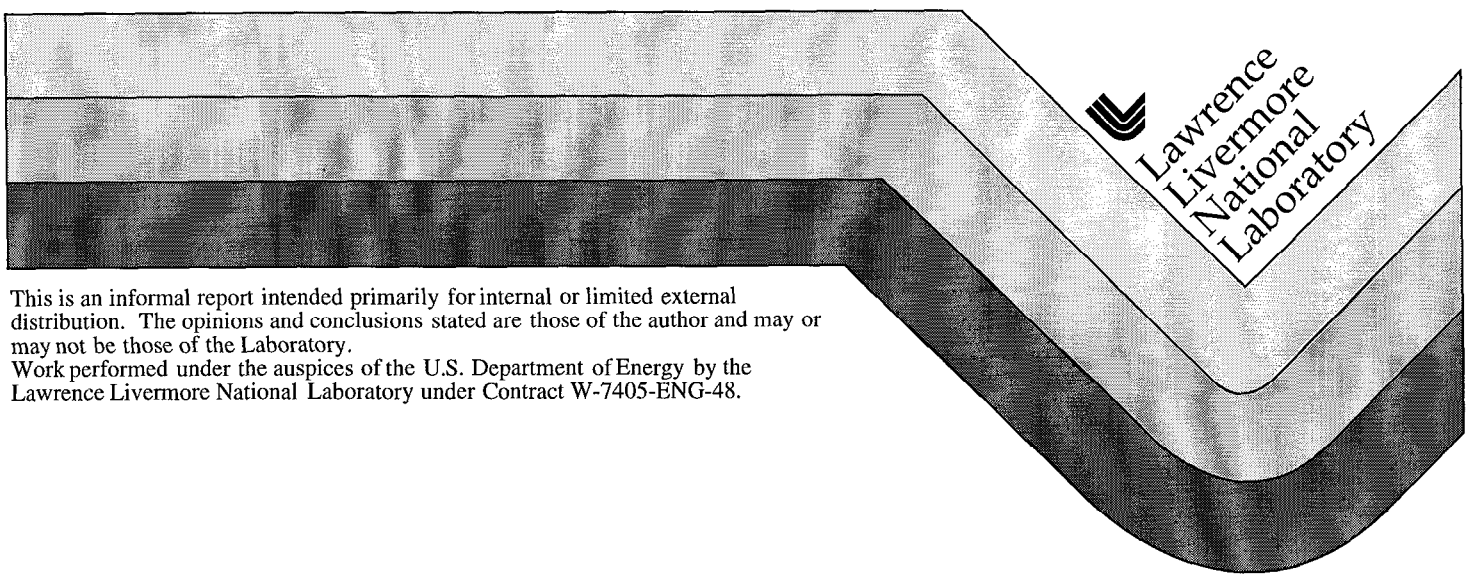

Work performed under the auspices of the U.S. Department of Energy by the Lawrence Livermore National Laboratory under Contract W-7405-ENG-48.

WBS: 1.2.3.12
QA: L

Civilian Radioactive Waste Management System
Management & Operating Contractor

Fracture/Matrix Flow Experiments Results

BA0000000-01717-5700-00008, Draft B

September 30, 1998

Prepared for:

TRW Environmental Safety Systems Inc.
1261 Town Center Drive
Las Vegas, Nevada 89134-6352

Prepared by:

Lawrence Livermore National Laboratory
P.O. Box 808
Livermore, California 94551-0808

Under Memorandum Purchase Order
HD2979KR5X

Civilian Radioactive Waste Management System
Management & Operating Contractor

Fracture/Matrix Flow Experiments Results

BA0000000-01717-5700-00008, Draft B

September 30, 1998

Prepared by:

Name _____ Date_____

Name _____ Date_____

Approved by:

Name _____ Date_____

Name _____ Date_____

UCRL-ID-131775

Fracture/Matrix Flow Experiments Results

by

Dorthe Wildenschild (LLNL)
M. S. Costantino (LLNL)
Jeffery J. Roberts (LLNL)
Timothy J. Kneafsey (LBNL)
Wunan Lin (LLNL)

Lawrence Livermore National Laboratory
Livermore, California
and
Lawrence Berkeley National Laboratory
Berkeley, California

W.B.S. 1.2.3.12
SP4CK1M4
BA0000000-01717-5700-00008 Draft B

September 30, 1998

This work was supported by a grant from the Geosciences Research Program, Office of Basic Energy Sciences of the Department of Energy and by the Yucca Mountain Site Characterization Project.
Work performed under the auspices of the Department of Energy by the
Lawrence Livermore National Laboratory under Contract W-7405-Eng-48

Contents

Tables

Figures

Abbreviations and Acronyms

LBNL	Lawrence Berkeley National Laboratory
LLNL	Lawrence Livermore National Laboratory
QA	Quality Assurance
REE	rapid evaporation events
YMP	Yucca Mountain Site Characterization Project

Acknowledgments

D. Rikard, D. Ruddle, P. Gaughan, J. Johnson, P. Harding, and S. Fletcher provided technical support. We thank Dan Schneberk for valuable discussions and ideas. This work is a collaborative effort.

Quality Assurance Information

This section addresses the acceptance criteria for the Level 4 deliverable *Fracture/Matrix Flow Experiments Results*. **Table 1** is the required "roadmap" that indicates where the criteria are met in this report.

Table 1. "Roadmap" table identifying where acceptance criteria are met in the deliverable *Fracture/Matrix Flow Experiments Results*

Criterion	Section
Conduct elevated-temperature enhanced-vapor-diffusion experiments to assess the importance of this heat-transfer mechanism	Chapter 1
Conduct elevated-temperature fracture-flow—capillary-imbibition experiments using x-ray and video-imaging techniques to provide phenomenological information on fracture–matrix coupling behavior	Chapter 2

Executive Summary

Water flow in the near-field environment is affected by coupled thermal-mechanical-chemical processes. Each of these contributes to minimize the energy of the physico-chemical system. The experiments described in this report address three important aspects of this coupled process: 1) the increase in the total thermal conductivity of the rock/water system caused by advective heat flow by the vapor phase; 2) the dynamics of the liquid and vapor water flow in a region containing the liquid–vapor isotherm; and 3) the recursive effect of solution chemistry on permeability and the thermal field.

Chapter 1 is a description of the first laboratory measurements of total thermal conductivity on the Topopah Spring welded tuff as a function of temperature, water-vapor pressure, and saturation. At the higher water-vapor pressures characteristic of regions with $T > 100°C$, measurements in soils indicate the total thermal conductivity is enhanced by advective transfer of the latent heat of vaporization through the vapor phase. Enhancement of the total thermal conductivity of the near field owing to this mechanism would have a first-order effect on the temperature field, and must be included in model calculations.

The potential enhancement of thermally driven water-vapor diffusion was investigated using a transient state thermal conductivity measurement. Thermal conductivity was measured as a function of pressure, temperature, and water content by the method of Parikh et al. (1979, pp. 1050–1052), which allows separation of the thermally induced latent heat transport contribution to the total thermal conductivity. The transient approach was tested on two reference materials, PTFE (Teflon™) and polycarbonate (Lexan™), and was found to yield thermal conductivities within 8% and 15%, respectively, of the manufacturer's values, with a measurement precision of about 1.5%. Our measured thermal conductivities are in general agreement with existing values at ambient pressures over a range of water saturations: the thermal conductivity of Topopah Spring tuff ranged from 0.94 to 1.97 W/m·K and showed an increase with increasing temperature above approximately 40°C. These values are slightly lower than the range of values (1.49–2.29 W/m·K) measured at similar conditions for other samples from the site. Our measurements indicate there is no enhancement of the total thermal conductivity in Topopah Springs tuff over our pressure–temperature–saturation range.

Chapter 2 is a description of the phenomenology of water flow in an initially unsaturated Topopah Spring tuff at $T > 100°C$ using three concurrent imaging techniques. The images obtained in this work provide dramatic visualization of the coupling between the geometry of the flow paths, the thermal field, and solution chemistry. They validate the generally held conclusions that 1) water flows along paths of least resistance; 2) high water flow rates cool regions below the boiling point; 3) high porosity clasts are capillary barriers to water transport; and 4) refluxing of solute-containing water deposits the solid phase solute, decreasing the permeability.

The penetration of liquid fingers into boiling regions in the near field has important consequences for repository design because flow may ultimately contact waste packages. An x-ray radiography method was developed to produce images of the flow of liquid in fractures and imbibition into the unsaturated matrix in tuff. Experiments were performed using various thermal gradients and flow rates. Concurrent with x-ray attenuation monitoring, video recordings and spatially resolved thermal-image recordings were made. Together these measurements provide information to investigate:

- Seepage into a heated natural fracture at different flow rates
- Finger and film penetration into the boiling region
- Liquid flow phenomena in a fracture and simultaneous imbibition into the rock
- The effects of boil-out and imbibition in a fracture model

The distance that liquid penetrates the boiling region was found to be sensitive to flow rate: during the highest-flow experiment, liquid water penetrated the entire fracture and continued to pass through the boiling region. Liquid-flow mechanisms observed include continuous and intermittent rivulets, films, and imbibition. These mechanisms were influenced by the application of heat and by the precipitation of salt, both of which hindered liquid flow. Rapid evaporation events (REEs) were frequently observed, with pressure pulses observed at distant locations.

1. Experimental Tests of Enhancement of Thermal Vapor Diffusion in Topopah Spring Tuff

by Dorthe Wildenschild, Jeffery J. Roberts, and Wunan Lin

1.1 Introduction

The impact of vapor diffusion and its potential enhancement are of concern with respect to the performance of the potential nuclear waste repository at Yucca Mountain. Under non-isothermal conditions, such as those prevailing in the near-field environment, gas-phase diffusion of water vapor (a condensable component) may be enhanced as compared to isothermal conditions. Two main phenomena are responsible for this enhancement (Philip and DeVries 1957, p. 226). Normally, diffusive transport of water vapor is obstructed by the presence of liquid islands in the pore throats, and diffusion is reduced at higher saturations. However, under a thermal gradient, a vapor-pressure gradient develops in the gas phase, causing water to evaporate from one side of the liquid island and to diffuse in the gas phase to a liquid island of lower temperature, where it condenses (**Figure 1**). Water flows through the liquid island as a result of differences in meniscus curvature between the two sides. This difference is caused by the temperature gradient between the liquid-vapor interfaces on the two ends of the liquid island. The evaporation–condensation process repeats itself on the other side of the liquid island; the result is an enhanced diffusive flux through the medium.

Figure 1. Liquid film between two soil grains forming a barrier to vapor transport

The second enhancement mechanism proposed by Philip and DeVries (1957, p. 227) relates to the use of an average temperature gradient in Fick's law. The thermal conductivity of the solid phase is very much greater than that of the liquid phase, which in turn is very much greater than the thermal conductivity of the air phase. Therefore, the mean thermal gradient averaged over all three phases is smaller than the temperature gradient across the vapor-filled pores. Water vapor moves primarily through the air spaces where the higher local thermal gradient provides a driving force for the diffusion of water vapor.

Thus far, thermally driven enhancement of vapor diffusion has only been quantified for soils (Cass et al. 1984, pp. 25–32). Other investigators (Cary and Taylor 1962, pp. 413–420; Hopmans and Dane 1986, p. 193) have suggested that thermally driven enhancement may be the cause of unexpectedly high thermal conductivities measured in soils. The objective of the present study is to test whether enhancement also takes place in rocks, specifically in the welded Topopah Spring tuff present at Yucca Mountain. Also, if the phenomenon does exist in rocks, we intend to quantify it using the transient method of Cass et al. (1984, pp. 25–32) described in the following subsections.

1.2 Theory

In a system of rock, water (liquid and vapor), and air, if the flux of liquid water is negligible, the heat flux density J_h is given by DeVries (discussed in Cass et al. 1984, p. 28 as Eq. 18) as

$$J_h = -(k_c + k_v)\nabla T, \tag{1-1}$$

where k_c is the thermal conductivity due to conduction and k_v is the thermal conductivity resulting from the transfer of latent heat through vapor diffusion. The thermal conductivity $(k_c + k_v)$ is calculated from the thermal diffusivity as

$$k = (k_c + k_v) = C_v \alpha . \quad (1\text{-}2)$$

C_v is the volumetric heat capacity (J/cm^3K) for the materials involved. ($C_v = \rho_{b,rock} c_{rock} + \rho_w c_w \theta$, where ρ and c refer to bulk density [kg/m^3] and specific heat [$J/kg \cdot K$] of rock and water, respectively, and θ is the prevailing water content. The contribution from the air phase is considered negligible.) α is the diffusivity, which is obtained by the method of Parikh et al. (1979, p. 1051),

$$\alpha = -(b \cdot 2.303 r^2)/X_i , \quad (1\text{-}3)$$

where r is the radius of the sample and b is the slope of a line fitted to a semilog-plot of time versus relative temperature change $T' = (T_2 - T)/(T_2 - T_1)$. T_1 and T_2 are temperatures of water baths used in the experiment such that $T_2 - T_1$ represents the maximum temperature change. The constant X_i has a limiting value of 2.405. The error introduced in α by using this value was estimated by Chung and Jackson (1954, p. 2563) to be less than 1% for relatively low water velocities, and this error decreases with increasing water velocity.

In order to quantify the potential enhancement of vapor diffusion, knowledge of the pressure dependence of k_v (dk_v/dP_r) is required. P_r is reciprocal relative pressure P_o/P, where P_o is atmospheric pressure and P is the gas phase pressure at which the measurement is taken. Cass et al. (1984, pp 25–32) calculated two types of enhancement factors, defined by Philip and DeVries (1957, pp. 222–232) and Cary and Taylor (1962, pp. 413–420) as the *mechanistic* and the *phenomenological* enhancement factors, respectively. The thermal conductivity k_v is not directly measurable; however, k_v is pressure-dependent, whereas k_c is not. Thus, measuring the pressure dependence of $k_c + k_v$ provides a method of separating k_c from k_v.

At infinite relative pressure (i.e., $P_r \rightarrow 0$) the vapor flux and, therefore, its associated latent heat flux is zero, and thus, $k_c + k_v$ is equal to k_c. We refer to Cass et al. (1984, p. 28) for the theoretical details. As enhancement presumably only takes place at intermediate water contents and possibly only in certain temperature ranges, we measured thermal conductivity as a function of both temperature, water content, and pressure.

1.3 Experiments

The sample originates from the Tsw2 unit of the Topopah Spring Member. This unit covers a depth range from 211 to 416 m. The 2.54-cm-diameter core used for this experiment is #01002186 (129.6-.7A) and was cored as a subsection of a larger core. Before use, a 1/16" hole was drilled in the center of the core for insertion of a thermocouple.

Using the method of Parikh et al. (1979, pp. 1050-1052), a right circular cylinder rock core was placed in a water bath, allowed to reach equilibrium at the temperature and pressure of that bath, and then moved to another water bath of different temperature. The resulting temperature change in the middle of the core was monitored with a thermocouple as a function of time. We repeated this procedure for a series of temperatures, pressures and water contents, to estimate the ratio dk_v/dP_r and thus the degree of enhancement under different circumstances. Only small temperature changes were used (approximately 5°C) to

keep the thermal gradients relatively small and thus minimize water redistribution in the core. By using two water baths at marginally different temperatures this precaution can be satisfied, yet thermal conductivities and associated enhancement coefficients can be measured over a wide range of temperatures (e.g., from ambient to 100°C). As shown in **Figure 2**, a 2.54-cm-diameter, 5.08-cm-long core sample was mounted in a thin-walled stainless steel cylinder and clamped between steel end plates. Prior to the tests on the tuff sample, we conducted tests on two plastic materials (Lexan™ and Teflon™) with and without the steel cylinder and obtained practically identical results. Thus, we assumed good contact between the samples and the cylinder, and no thermal couplant was used in the experiments to facilitate heat flow through the narrow gap.

Figure 2. Schematic of the pressure cell holding the rock core

Polycarbonate end caps are used at the contact surface between stainless steel and rock core to minimize heat transfer through the end planes. We used mixers to keep the water moving in the baths and to avoid an increase in water temperature in the immediate vicinity of the sample. To keep evaporation at a minimum, polyurethane balls covered the water surface. The thermal diffusivity and, thus, the thermal conductivity were obtained from the transient response of the thermocouples as explained in Section 1.2. Once the thermal conductivity was determined, the enhancement coefficients could be obtained as described in Equations (25) and (28) in Cass et al. (1984, p. 28).

1.4 Results and Discussion

1.4.1 Test of the Transient Method on Lexan and Teflon

The method of Parikh et al. (1979, pp. 1050–1052) was tested on two materials, polycarbonate (Lexan™) and PTFE (Teflon™). The materials were machined to fit in the stainless steel cylinder as tightly as the tuff sample (diametric clearance less than 0.08 mm). Experiments were carried out the same way as for the rock, except that these materials were dry at all times. We conducted four heating and four cooling tests; the averaged results of these tests are presented in **Table 2.**

Table 2. Results of test of method on Lexan and Teflon

Material	*k* (Measured) (W/m·K)	Measurement Precision (%)	*k* (Mfr.'s Value) (W/m·K)	Difference (%)	Source of Manufacturer's Value for *k*
Lexan™	0.219	1.5	0.19	15.3	http://www.centor.com/cbmat/visitors/00456.html
Teflon™	0.248	1.6	0.23	7.8	http://www.fietz.de/wst1e.htm

As seen in Table 2, the measured thermal conductivities of the reference materials were measured very accurately, with an error of only 1.5 and 1.6%. Consecutive measurements showed the method to be repeatable and precise. The reference values of thermal conductivities for these materials were taken from the manufacturers' Web sites; they were not measured for the actual samples used. The differences between the measurements and the published reference values of 15.3% and 7.8% are therefore not surprising, and our results indicate that the method of Parikh et al. (1979, pp. 1050–1052) is adequate for thermal conductivity measurements.

1.4.2 Thermal Conductivity of Topopah Spring Tuff

The thermal conductivity of Topopah Spring tuff was measured for a range of temperatures (22.5, 27.5, 42.5, 57.5, 72.5, and 87.5°C), pressures (0–250 psi), and saturations (0.097, 0.20, 0.36, 0.58, and 0.76). The measurements presented here represent these five saturations; corresponding water contents were obtained from a porosity of 0.083 (cm^3/cm^3). The measured conductivities vary between 0.94 and 1.97 W/m·K and increase with temperature above approximately 40°C for all five saturations (**Figure 3**), reflecting a similar relation between specific heat and temperature. The specific heat used for calculating the thermal conductivity was measured (PMIC 1998, pp. 1–6, DTN LL980916204242.056) and was found to vary with temperature between 0.81 and 1.43 J/g·°C.

Figure 3. Thermal conductivity of Topopah Spring tuff as a function of temperature and pressure

(a) for saturation S_w = 0.097 (water content θ = 0.008 cm^3/cm^3) (DTN LL980916104242.052)

(b) for saturation S_w = 0.20 (water content θ = 0.017 cm^3/cm^3) (DTN LL980916104242.052)

(c) for saturation S_w = 0.36 (water content θ = 0.030 cm^3/cm^3) (DTN LL980913104242.051)

(d) for saturation S_w = 0.58 (water content θ = 0.048 cm^3/cm^3) (DTN LL980916104242.052)

(e) for saturation S_w = 0.76 (water content θ = 0.062 cm^3/cm^3) (DTN LL980916104242.052)

As seen in Figure 3a–e, the temperature dependence is consistent for all saturations and pressures from 0 to 250 psi. We measured the maximum thermal conductivity as 1.97 W/m·K at a saturation of 0.76 corresponding to a water content of 0.062 (cm^3/cm^3), while the minimum value of 0.94 W/m·K was measured at a saturation of 0.36 with a water content of 0.030 (cm^3/cm^3). All five curves show very similar variation with temperature, whereas an increasing variation with pressure is observed with increasing saturation.

In comparison to our measurements, low-temperature (< 100°C) thermal conductivity for field samples from the Yucca Mountain tuff unit Tsw2 was measured by Brodsky et al. (1996, p. 32) to be 2.29 W/m·K at saturation, 1.66 W/m·K air dry, and 1.49 W/m·K for dry samples. The thermal conductivities measured in our study are slightly lower than this range of conductivities. The differences in thermal conductivity might be due to several factors, including sample heterogeneity (porosity, mineralogy), saturation, and temperature. Also, the values listed by Brodsky et al. (1996, p. 32) have rather large standard deviations. The increase in thermal conductivity with temperature is, however, not present in situ.

1.4.3 Enhancement of Water Vapor Diffusion

The thermal conductivity is plotted as a function of reciprocal relative pressure P_r in **Figure 4** to assess the existence of enhancement. A positive slope ($d(k_c + k_v)/dP_r > 0$) in this figure indicates enhancement ($dk_v/dP_r > 0$) because k_c is pressure-independent. As seen in Figure 4, there is most likely no enhancement taking place at this water content for any of the temperature intervals investigated. Very similar curves were found for all the investigated water contents, leading us to conclude that the process of enhancement of vapor diffusion is insignificant in this material for the conditions investigated.

Figure 4. Thermal conductivity of Topopah Spring tuff as a function of temperature and reciprocal relative pressure for S_w = 0.36 (θ = 0.030 cm^3/cm^3) (DTN LL980913104242.051)

We are performing measurements on a sand–clay mixture to validate our measurement and estimation approach. Preliminary results of these investigations indicate that it is possible, using this methodology, to observe enhancement of vapor diffusion in the sand–clay mixture, of a magnitude similar to the enhancement observed by Cass et al. (1984, p. 29).

2. Fracture/Matrix Flow Under a Thermal Gradient: Experimental Observations Using X-Ray Radiography, Visual Imaging, and Thermal Imaging

by Jeffery J. Roberts and Timothy J. Kneafsey

2.1 Introduction

Understanding and predicting the performance of a high-level nuclear waste repository requires knowledge of how water flows through heated, unsaturated, fractured rock. Several strategies and models for the isolation of waste packages and containment vessels from infiltrating liquid water and condensate from steam have been proposed (e.g., Buscheck and Nitao 1992, pp. 1003–1017). These strategies depend to some degree on flow in fractures under thermal gradients and the effect of matrix imbibition on fracture flow (Wilder 1996, Chapter 1). The distance that water can travel during gravity-driven fracture flow is controlled by several factors, including the saturation of the matrix, the fracture aperture, the capillary properties of the matrix, and the temperature of the rock (Nitao and Buscheck 1991, pp. 2099–2112). Flow in fractures can be slowed by matrix imbibition that is driven by capillary suction. A theoretical investigation of liquid flow and infiltration into heated rock has been reported by Phillips (1994; 1996, pp. 1665–1670). Phillips shows that the depth of penetration of liquid fingers into superheated rock depends on several factors, including flux, thermal conductivity of the rock mass, and the temperature gradient. In the present work, a series of experiments has been performed to investigate fracture flow and fracture-matrix interactions under a thermal gradient.

To observe phenomena that occur when water is introduced into a fracture containing regions at temperatures exceeding the boiling point of water, two experiments were conducted in which water containing 5% potassium iodide (to enhance x-ray attenuation) was introduced into a fracture composed of a saw-cut piece of Topopah Spring tuff and a glass plate. Visual information was gathered with a video camera; temperature information of the front glass face was gathered with an infrared camera; temperature data from within the rock was collected using thermocouples; and information on imbibition into the rock and precipitation of potassium iodide crystals was obtained through x-ray attenuation.

These experiments were conducted in collaboration with T. J. Kneafsey at Lawrence Berkeley National Laboratory (LBNL). Visual and infrared information was collected by LBNL under LBNL's Yucca Mountain Site Characterization Project (YMP) Quality Assurance (QA) Program. Sample preparation, assembly construction, x-ray attenuation measurements, and thermocouple temperature measurements were performed under Lawrence Livermore National Laboratory's (LLNL) YMP QA Program. Information resulting from tasks performed under LBNL QA are presented courtesy of T. J. Kneafsey. Further interpretation of this data will be submitted by LBNL in milestone SP3CK1M4.

Further data analysis and calculations to aid interpretation, understanding of physical processes, and the relation to repository modeling are beyond the scope of this report.

2.2 Experimental Methods

2.2.1 Sample Preparation

A block of Topopah Spring tuff (SPC 00504573.3) collected from Fran Ridge (near Yucca Mountain, Nevada) was ground into a 14.94 x 22.96 x 2.62 cm^3 block. The surface to be mounted next to the glass plate was beadblasted to roughen it slightly. The sample was ultrasonically cleaned with water and dried in a vacuum oven at 35°C for about two weeks. During this time period the weight was periodically monitored and when it did not change appreciably for several daily weighings, the sample was assumed to be dry. The back, top, and side surfaces were coated with a heat-resistant room-temperature vulcanizing (RTV) compound (Allguard Elastomeric Coating). The block was installed in an aluminum frame (**Figure 5**) with a 6.35-mm-thick borosilicate glass window of dimensions 13.1 × 25.4 mm. Gold shims (~12.5 μm thick) separated the rock from the window, creating a nominal aperture of 12.5 μm. Two 25-W strip heaters were mounted across the back of the frame. Two 50-W cartridge heaters were installed in boreholes centered (back to front) in the rock about 2.25 cm above the bottom of the rock, and one 25-W and two 10-W strip heaters were installed below an aluminum plate in thermal contact with the bottom of the sample. Channels were machined in the aluminum plate to enable water flowing the length of the fracture to exit the sample to a lower collection chamber. Each heater combination had a separate power supply so that by varying the power to each an even temperature distribution could be achieved. Type J thermocouples were placed near the heaters (Thermocouples 1–3), on top of the rock near the fracture (13), and into the rock (4–12), to monitor temperature. Thermocouples 4 through 12 were installed centered in the one-inch thickness of the rock, penetrating the width of the sample to a depth of 4.7 cm. The matrix porosity, as determined by gravimetric methods, of four core samples taken adjacent to the block, was 9.2 ± 0.4%. Based on other porosity measurements on numerous samples from the same block of tuff (gravimetric and mercury-injection porosimetry), we assume the overall porosity of the sample to be ~10%. Because of local heterogeneity, a more precise estimate of porosity is not warranted.

At the top and bottom of the sample were chambers for ponding and collection of water. At the top of the sample, the chamber was filled with a Teflon™ block machined to allow free access of water to the fracture aperture. Water could not enter the sample from the top, but had to flow into the gap between the rock and the glass plate before it could be imbibed into the matrix. The space-filling Teflon also served to limit the volume of water that the top chamber could hold, lowering the time between the pump being turned on and water beginning to flow into the fracture.

After assembly the sample was stored in a vacuum oven at 35°C to prevent moisture uptake from the atmosphere. We assume an initially dry condition.

Figure 5. Experimental apparatus

2.2.2 Method

The sample was heated throughout the experiment. Changes in power output to each heater or set of heaters were made to control temperatures and the temperature gradient in the rock. Water was not introduced into the fracture until the temperature at Thermocouple 6 had reached a steady value near 102°C in the first experiment, 110°C in the second. Water containing potassium iodide (5% by weight) was introduced through the inlet tube at

2.5 ml/min for 20 min, 1.18 ml/min for 55 min, and 0.55 ml/min for the remainder of the first experiment (0.3 ml/min for the duration of the second experiment). Potassium iodide is added to the water to increase x-ray attenuation. Previous radiographic fracture-flow experiments used a solution of 10% KI by weight (i.e., Roberts and Lin 1996, pp. 89–91; Roberts and Lin 1997, pp. 1–10); however, the high salt content can cause excessive crystal deposition in the boiling region. For this set of experiments the salt content was reduced to provide the best balance between x-ray attenuation contrast and limited salt deposition.

2.2.3 Images

X-Ray Images

X-ray radiographs were taken periodically to record water movement into the fracture and rock matrix by moving the sample vertically through the linear x-ray source (160-kV Comet x-ray tube with IRT Controller and 0.4-mm copper filtration; Parker Compumotor 4000 stage). X-rays passing through the sample were converted to a digital signal by a photodiode linear array detector (Thomson Linear Detector Array THX 1080) and stored by computer. Pixel size is ~450 × 500 μm including a magnification of 1.144. Water was ponded on the top of the upper fracture surface and allowed to flow down the fracture while x-ray radiographs were periodically taken to record water movement in the fracture and matrix (**Figure 6**). X-ray images were taken on a time-scale determined by the rate at which changes could be observed in the sample. Generally, images were taken as quickly as possible at the beginning of an experiment, while at later times as much as 4–12 hours lapsed between x-ray images. For these two experiments, water entered the sample only through the top fracture area (the rest of the sample top area was sealed).

X-ray images were generally analyzed by simple difference imaging. The difference image method consists of taking background radiographs of the sample in an initial known state (typically dry or fully saturated). After imposing some change on the sample such as liquid flow, or heating or cooling, changes from the initial state can be observed by subtracting the initial image from the subsequent images. Difference imaging permits the qualitative imaging of spatial and temporal variations of saturation in the matrix. More quantitative evaluations of saturation are performed by a similar procedure described in detail by Roberts and Lin (1997, p. 482 and CD-ROM). Most flow and imbibition phenomena and processes can be observed through difference imaging.

For all the x-ray images shown here, darker colors indicate higher attenuation and lighter colors indicate lower attenuation. In the case of difference images, higher attenuation generally indicates the addition of material, either KI-bearing water or solids precipitated out of solution (such as KI crystals).

Figure 6. **Schematic of x-ray radiograph system**

Sample translates vertically through the 160-kVp linear source. Detector stores digital data, line by line. One scan takes between one and two minutes, depending on sample height. Thermal and video imaging were concurrent.

Visual Images

Video imaging was performed with reflected room light using a Sony CCD RGB color video camera (model DXC-151, SN 10062) and recorded on a Toshiba 24-Hour Security

Recorder Time Lapse VCR (model KV-5124A, SN3020588). Video time codes provide time measurements on time scales not recorded manually.

Infrared Images

Temperature images were made with an infrared camera (Inframetrics PM 200 Thermacam SN 8954 in Experiment 1 and Inframetrics PM380 Thermacam SN 18132 in Experiment 2), captured on video from the "Tgram" camera output (Sony Handicam), and interpreted by the ThermaGRAM 95 1.30 program (Thermokinetix Systems Ltd., Mount Pleasant House, Mount Pleasant, Cambridge, CB3 ORN, UK). Data were downloaded in Instrument Units (IU) into an ASCII file, which was imported into an Excel 5 spreadsheet for calibration. Calibration curves were generated by comparing camera output against a thermometer calibrated according to YMP-LBNL quality-assurance procedures (4/2/98 to 5/6/98 calibrations for Experiment 1 and 7/3/98 to 7/15/98 calibrations for Experiment 2). The interpolation range of these calibrations is approximately 72–99°C. Temperatures outside of this range require extrapolation. Because the transmissivity of infrared energy by glass is low, these images are assumed to be of the temperatures of the front glass surface.

Boiling Temperature

Because the water used in this experiment could hold a substantial amount of potassium iodide, the boiling temperature could vary within the assembly and range from near 100°C to 106°C. The boiling-point elevation is calculated by taking the boiling-point elevation coefficient for water (0.512°C) (Lide 1990, p. 15-11) and multiplying it by the number of gram-molecular weights of potassium iodide per 1000 g of water. The solubility of potassium iodide in hot water (100°C) is 208 g/100 cc water (Lide 1990, p. 4-92), and the molecular weight is 166. Thus the boiling point is raised by 6.41°C for a saturated solution. The boiling-point elevation for a 5% potassium iodide solution is 0.15°C. Atmospheric pressure was not monitored.

2.3 Results of Previous X-Ray Radiography Experiments

A series of experiments similar to those described above was performed on several samples under a variety of conditions (Roberts and Lin 1996, pp. 89–91; 1997, pp. 1-10); these experiments are briefly described here so they can be compared with the present experiments. Sample sizes and initial conditions may have been different, as well as the sample holder design. These experiments included:

(1) Fracture flow and imbibition with nominal normal stress on an unshimmed fracture (23°C, sample initially dry, water ponded on top)

(2) Fracture flow and imbibition with 25-μm-thick shims placed in the fracture (23°C, sample dried after (1), water ponded on top)

(3) Dehydration of the sample after (2) under a thermal gradient created by imposing temperatures of ~95°C at the bottom and ~33°C at the top

The primary differences between the previous and current experiments are:

- The orientation of the sample with respect to the x-ray image
- The size (lateral extent) of the fracture
- Analysis of a tensile fracture versus a saw-cut/glass bounded fracture
- Concurrent thermal and video images

Previous experiments were performed with the fracture perpendicular to the image plane. The advantages are that the fracture has tuff on both sides and it is easier to image matrix imbibition from the fracture using x-ray radiography. The present combined-imaging experiments benefited from a larger fracture surface area and the added information obtained by the different imaging methods.

2.3.1 Fracture Flow

Imbibition occurred chiefly through the matrix for the unshimmed fracture experiment, and primarily horizontally from the fracture to the matrix during the shimmed fracture experiment. A roughly v-shaped wetting front was observed for the unshimmed case, and after more than 2017 hours of ponding, water still had not flowed the length of the fracture. During the shimmed fracture experiment, water flowed the fracture length after only ~0.15 hours. Different (lateral) imbibition rates were observed in different regions of the sample, demonstrating the heterogeneous properties of the rock. Enhanced imbibition appeared to be controlled by the presence of lithic fragments that contain small microfractures. A significant difference in the two series of experiments is that water was imbibed laterally into the matrix (from the fracture) at a much higher rate when the fracture was shimmed open. For the shimmed experiment, after 1000 hours a large portion of the sample was highly saturated.

The dehydration experiment (3) began after no more imbibition into the matrix was observed (shimmed experiment, > 1200 hours of imbibition). Dry-out along the fracture was observed and was most pronounced between 4.5 and 23 hours after heating was initiated. At longer times dry-out along the fracture was not apparent, and at times greater than ~215 hours the fracture was highly attenuating. Possible explanations include:

- The fracture increased in saturation at times greater than 215 hours, or
- Evaporation of water continuously along the fracture resulted in the crystallization of salt (KI) that attenuates the x-rays.

Another feature was the development of a horizontal band of high attenuation approximately 1.5–2 cm from the bottom of the sample. This band appeared initially at about 0.5 hours after heating and became more pronounced with time. At about 25 hours after heating, two such bands were observed, again near the bottom of the sample.

2.3.2 Fracture Flow Under a Thermal Gradient

Two previous experiments will be described here in some detail because of their relevance to the present study: FR5 and FR6 (**Table 3**). Refer to Roberts and Lin (1997, pp. 1–10) for details. These experiments are similar to the others mentioned above except that the temperature field and gradient is better controlled. FR5 had a temperature of ~111°C at the bottom and ~28°C at the top, and FR6 had a temperature ~148°C at the bottom and ~80°C at the top. The boiling region (T > 100°C) extended 2–3 cm into FR5 (from the bottom) while FR6 had a much larger boiling region extending 6–7 cm into the sample (from the bottom). Two experiments were performed on FR6, one with a hydrostatic head of ~1.45 m, and another with the head approximately 2.92 m. The head on FR5 was quite small, only 1–2 cm, which was the chamber height where the water ponded on top of the sample.

Table 3. Experimental parameters (DTN LL980916004242.055)

Sample/Run	Number of Heaters	Bottom Temp. (°C)	Top Temp. (°C)	Water Column Height (m)
FR5	3 (bottom heat only)	111	28	0.02
FR6	7 (four side heaters)	148	80	1.45
FR6b	7 (four side heaters)	148	80	2.92

Results for experiment FR5 are shown in **Figure 7** (Roberts and Lin 1997, pp. 1–10). These images are difference radiographs, and for the images shown here, darker shades indicate higher attenuation and, hence, indicate the presence of water (or possible KI precipitation or increased concentration). Figure 7a shows the progress of the wetting front in the matrix and the fracture 1.7 hours after water was ponded on the top surface. The fracture is near the center of the image. The flow reached ~13 cm down the fracture relatively quickly, and then stopped. The most likely reason for the stopped flow is the presence of a relatively high-porosity clast that is intersected by the fracture. As time progressed, this more porous region became more saturated until flow proceeded around or through the region. During this time there was significant lateral imbibition into the matrix from the fracture. The extent of this can be seen in Figure 7b, taken 73.5 hours after ponding. Figure 7b still shows the highly attenuating spot where flow stopped and another highly attenuating region near the bottom of the sample. After flow continued past the highly porous region, the shape of the wetting front was less sharp and more rounded. This wetting front stopped ~2.6 cm from the bottom of the sample. A very narrow neck of high attenuation extended downward from this section to the lowermost highly attenuating region at the bottom of the sample. In this sample the lowermost 1–2 cm are above boiling. Our interpretation is that the highly attenuating spot at the very bottom of the fracture is a region where KI crystals may have deposited because of continued boiling. For this experiment, liquid water never penetrated the entire fracture length. After nine days the heaters were turned off and water still did not flow through the fracture.

Figure 7. **Difference radiographs of FR5 (DTN LL980916004242.055)**

Darker shades indicate increased x-ray attenuation compared to the initial image, and hence, increased saturation. Images were taken 1.7 (a) and 73.5 (b) hours after flow was initiated. The first image shows a stoppage of flow along the fracture caused by the presence of a relatively porous region intersected by the fracture. The second image shows progression of the wetting front past the highly porous region to the boiling zone.

Figure 8 shows two difference images for experiment FR6 and FR6b. These two experiments were similar to FR5 except that FR6 was hotter, had less of a thermal gradient, and the column of water used to pond the sample was higher (Table 3). Figure 8a is an image of FR6 7.2 hours after ponding. Features indicated are rapid flow down the fracture that stops, development of a highly attenuating region, and the development of a narrow neck that is highly attenuating. Liquid water penetrated about 3 cm into the boiling region. The highly attenuating neck extending below the boiling region is unexplained. What is different about this experiment compared to FR5 is that flow continued down the length of the fracture after the heaters were turned off and the sample cooled. This is explained by either the increased head, or the lack of complete sealing of the fracture by crystal deposition.

Figure 8. **Difference images of FR6 (a) and FR6b (b), 7.2 and 0.67 hours after flow was initiated (DTN LL980916004242.055)**

Thermal gradient is indicated between the figures. The difference between these two experiments was the height of the water column, 0.26 and 0.46 m, for FR6 and FR6b respectively. The difference in head was large enough to force flow through the boiling region during FR6b.

Figure 8b shows an image of FR6b about 0.67 hours after flow was initiated. This sample had almost twice the head of FR6. The thermal gradient was the same, but in this case water flowed the entire length of the fracture within minutes and continued to flow through the boiling region. Thus we conclude that hydraulic head directly affects the distance liquid water can penetrate into the boiling region (refer to Phillips 1994; Phillips 1996, pp. 1665–1670).

2.4 Results and Discussion

2.4.1 Observations

Experiment 1

Seepage through the fracture aperture and imbibition into the rock occurred on very different time scales, with the initial seepage through the aperture occurring on an order of 10 minutes. Imbibition was noticed on a time scale of hours. A discussion of results from the three observation methods is presented below. A history of all the temperatures in the rock matrix (after heating) as recorded by Thermocouples 4 through 12 is presented in **Figure 9**. For both Experiments 1 and 2, **Table 4** shows the precise placement of the thermocouples and the pre-flow temperatures. For Experiment 1 we note that Thermocouples 4, 5, and 6 were above boiling.

Table 4. **Locations and pre-flow temperatures as recorded by Thermocouples 4–12 (DTN LL980916004242.055)**

Thermocouple	Distance from Bottom of Rock (cm)	Pre-Flow Temperature (°C)	
		Experiment 1	Experiment 2
TC 4	0.32	143.2	146.5
TC 5	3.12	141.9	146.1
TC 6	5.92	106.5	109.9
TC 7	8.72	97.1	100.0
TC 8	11.52	90.5	93.1
TC 9	14.32	84.4	86.6
TC 10	17.12	79.3	81.2
TC 11	19.92	75.5	77.2
TC 12	22.72	74.2	75.8

The initial condition of the rock and fracture and initial seepage are shown in **Figure 10**. The rock is physically heterogeneous on a small scale (order of centimeters) and contains a

teardrop-shaped darker region surrounded by a lighter region in the lower right. Some pore spaces in the lighter region are visible to the eye, and the porosity in these regions is visibly higher. Fractures are present in the rock, as well as pores on the millimeter scale and smaller.

Figure 9. Temperature history of Thermocouples 4–12, Experiment 1 (DTN LL980916004242.055)

Figure 10. Video images of initial condition and seepage in tuff/glass fracture, Experiment 1

In Experiment 1, water initially seeping into the aperture progressed downwards somewhat uniformly, with a stronger flow towards the center. Fingering occurred due to heterogeneities in the rock, with the dry regions between fingers wetting soon afterwards. As the water reached the warmer regions, the wetting became slower. A capillary barrier, formed by the higher porosity region surrounding the teardrop-shaped darker region (Figure 10a, bottom right), impeded flow into this region temporarily. At later times in the heated zone, white crystals of potassium iodide began forming. These became more prominent over time, with the salt crystals impeding flow.

The initial thermal image (**Figure 11a**) shows a distinct region above boiling in the lower third of the assembly. The shape of the hottest region is strongly influenced by the cartridge heaters, with a cooler ridge forming between the heaters. Temperatures at the top of the assembly are around 70°C. Upon introduction of water, fingers penetrated the boiling region, particularly in the center. The indicated temperatures in the location of the fingers exceed 100°C due to boiling-point elevation.

Figure 11. Initial and subsequent temperature distributions of the outer glass surface, Experiment 1

In Figure 11b (infrared), corresponding to **Figure 12b** (visual) and **Figure 13b** (x-ray), only a circular region on the left-hand side near the bottom is well above the boiling temperature (red–yellow region). In the same location in the visual image (Figure 12b), a dry region is visible, with potassium iodide crystals present. The right side is wet and near the water boiling point. Figure 13b, a difference image showing the x-ray attenuation at the indicated time subtracting out the x-ray attenuation of the rock in the starting condition, shows imbibition occurring (darker regions) primarily in the originally lighter colored (compare to Figure 10a) and presumably higher permeability regions of the rock.

Figure 12. Video images taken at the indicated times, Experiment 1

Figure 13. X-ray attenuation difference images indicating imbibition and potassium iodide precipitation over time, Experiment 1 (DTN LL980916004242.055)

Darker shades indicate more attenuation, thus more imbibition or crystal precipitation. In (d), circled areas are visible as precipitated potassium iodide in Figure 10.

In Figure 11c, following reduction of the inflow rate, larger above-boiling regions (red–yellow region) are observed on both sides, and the top of the assembly is slightly warmer than in Figure 11b. Figure 12c shows a region of white crystals on the bottom left, which is

presumably dry. On the bottom right, the above-boiling region is also visually distinguishable; however, it appears that the aperture is still wet. In Figure 13c, more imbibition is evident in the same regions where it was previously observed. In the lower part of the assembly near the heaters, imbibition and salt crystal deposition are responsible for the dark regions in the image.

In Figure 11d, the above-boiling regions are cooler (less red) than those in Figure 11c and are shaped differently. These boiling regions formed and disappeared throughout the duration of the experiment as liquid cooled them and flowed through the fracture there. In Figure 12d, two dry regions containing potassium iodide crystals are observed, but the apparent extent of the dry region on the left is smaller than in Figure 12c.

These white crystal-containing regions are also visible in the x-ray image (circled in Figure 13d) due to solid potassium iodide attenuating the x-rays. Comparing Figure 13d to Figure 13a, b, and c, imbibition is seen to be increasing over the entire block, but the strongest imbibition is occurring in the more permeable and porous regions.

Potassium iodide crystal buildup is apparent near the cartridge heaters.

In Figure 11e, only one region (on the right) strongly exceeds the boiling point. Vertical cool fingers streak through the original boiling-hot region. In Figure 12e, only a small whitish region is seen on the bottom right, corresponding to the hottest part seen in Figure 4e. In Figure 13e, imbibition has continued over the entire face, but it is greater in regions where previously observed. In the 18.5 hours between the images in Figure 13d and Figure 13e, extensive potassium iodide deposition has occurred in the boiling region.

As the experiment progressed, potassium iodide crystals built up at locations within the heated region, reducing the hydraulic conductivity of the fracture and impeding flow. Water was introduced at a constant rate, so that when the injection rate exceeded the hydraulic conductivity, the excess water flowed out the overflow tube on the assembly top. This tube was suspended from the ceiling, and as the flow was restricted, the head built up. The level in the overflow tube was intermittently monitored, and at one time, the level was about 2.03 m of water (and air bubbles) above the top of the assembly.

In the region near the cartridge heaters and below, the dried-out zone changed in shape and location through the course of the experiment. There were times when the right side was dry but not the left and vice versa, times when both were dry, and times when both were wet, indicating that flow through the heated region of the fracture was unsteady. In addition to this unsteady behavior that occurred when the x-ray stage was steady for long periods of time, the stage was lowered and raised during x-ray imaging, which caused alteration of shape and presence of the dry zones. Changes in head from raising or lowering the stage, head build-up, or vibration may have induced flow to break through a weaker physical and thermal boundary, re-dissolving previously precipitated crystals, opening the pathway and decreasing flow resistance. Once the built-up head decreased, slow boiling and precipitation again filled the aperture, impeding flow.

Rapid evaporation events (REEs) were frequently observed in the experiment in the boiling regions at the lower (heated) end of the assembly. Visually, the REEs occurred periodically on a time scale of tens of seconds. Often they would occur in the same region. It appears that small rivulets of water would feed into an area. Sufficient water collected and/or the water was superheated, at which point a region on the order of 1–2 cm diameter would "burst" into the gas phase. The effects of these bursts (i.e., pressure pulses) could be observed at distant regions of the sample. An additional effect of these REEs was that water

in the overflow tube at the assembly top rose and fell about 1 cm. This is a large margin considering the assembly configuration. The pulse, in that magnitude, had to be transmitted through the narrow aperture to that distant location, even though the outlet at atmospheric pressure is located only centimeters from where the REEs were occurring. More thorough analysis of these events will performed.

Experiment 2

After being cleaned, by repeated soaking in distilled water, and dried, the block of Topopah Spring tuff used above was replaced in the assembly shown in Figure 5.

The sample was heated throughout the experiment. Refer to Table 4 for pre-flow temperatures, and note that Thermocouples 4 through 7 were above boiling. Water was not introduced into the fracture until the temperature at Thermocouple 6 had reached a steady value near 110°C. Water containing potassium iodide (5% by weight) was introduced through the inlet tube at 0.3 ml/min for the duration of the experiment. This flow rate was selected to be lower than the minimum flow rate from the previous experiment. The temperature history for Thermocouples 4 through 12 is presented in **Figure 14.**

Figure 14. Temperature history for Thermocouples 4–12, Experiment 2 (DTN LL980916004242.055)

Again, seepage through the fracture aperture and imbibition into the rock occurred on very different time scales, with the initial seepage through the aperture occurring on an order of magnitude of tens of minutes even with the lower flow rate. Again, imbibition occurred on a time scale of hours. A discussion of results from the three observation methods is presented below. **Figure 15** shows the initial condition of the rock and fracture and initial seepage through the assembly, and **Figure 16**, **Figure 17**, and **Figure 18** compare images from five different times for each method.

Figure 15. Video image of initial condition, seepage, and condensation halo formation, Experiment 2

Arrows point to potassium iodide crystals.

Figure 16. Initial and subsequent temperature distributions of the outer glass surface, Experiment 2

Figure 17. Video images taken at the indicated times, Experiment 2

The wet-appearing band is indicated in (d). Arrows point to potassium iodide crystals.

Figure 18. X-ray attenuation difference images indicating imbibition and potassium iodide precipitation over time, Experiment 2 (DTN LL980916004242.055)

Darker shades indicate more attenuation, thus more imbibition or precipitation. Indicated areas are visible as precipitated potassium iodide in Figure 15.

Water initially seeping in the aperture progressed downwards in thin fingers, unlike the previous experiment. Upon reaching the hot rock, boiling occurred and a condensation halo

formed. A second finger formed from the top intersecting the first finger, and the condensation halo grew in the outline of the boiling region. Flow in fingers continued along the condensation halo and penetrated the boiling region. Boiling in the hot fracture was unstable, with REEs occurring frequently in the center and both sides. Additional fingers formed from other locations on the assembly top, and flow began to break through about one-half hour after the beginning of the experiment. REEs were frequently observed, and their effects were seen in the fracture, but no external indication of their pressure pulses was observed because no overflow occurred.

A boiling temperature gradient caused by a concentration gradient in the water is likely partially responsible for the wet-appearing band (Figure 17d) in the bottom of the assembly between the precipitating salt (lower white band, $T_{boiling}$ ~106°C) and the white band of condensation ($T_{boiling}$ ~100°C) on the glass several centimeters higher. The salt buildup generally is within the 120°C isotherm, but the condensation band is between the 95°C and 100°C isotherm. The condensation band was expected to be below 100°C because the temperatures monitored are that of the front surface of the glass in contact with the atmosphere. Temperature profiles from both the infrared measurements and thermocouples show a different slope in this region between the two bands. Strictly speaking, temperature measurements from the infrared camera are not calibrated above 99°C; however, these temperatures are in agreement with thermocouple data, which are valid above 99°C.

As the experiment progressed, water flowing around the heated region deposited potassium iodide in the fracture (Figure 15 and Figure 17). Two large washout events occurred when water remaining in the assembly below the rock boiled back up into the heated region, dissolving and partially washing out the salt deposited there. During these washout events, water was drawn out of the bottom and sides and from above into the hot region, moving crystals closer to the center of the hottest regions. Following the washout events, potassium iodide was again deposited in the aperture in nearly the same locations.

Infrared images show that the boiling region was initially peanut-shaped and smooth (Figure 16). Thin fingers penetrated the boiling region and began to cool it, and flow continued to cause local cooling and altering of the shape of the boiling region (Figure 16). In contrast to Experiment 1, flow through the hottest regions was not from above, but occurred during intermittent washout events from below.

Imbibition was strong where it was noted in Experiment 1, around the teardrop-shaped region, and lighter colored porous regions in the rock (Figure 18). Potassium iodide crystals are visible in the x-ray images at the bottom (compare to Figure 17). Imbibition continued as the experiment continued (Figure 18), with x-ray attenuation, which accounts for both imbibition and salt deposition, being largest above the cartridge heaters in porous regions of the rock.

2.4.2 Discussion

Water flow through the boiling region in the rock-glass fracture assembly was strongly influenced by the application of heat and precipitation of solute. Both heat and precipitated materials impeded the flow of water. Both of these barriers were penetrated intermittently, because of movement and head buildup in Experiment 1 and because of washout events in Experiment 2.

Under steady heat and water application rates, steady flow was not observed within the time scale of the experiment. Intermittent flow occurrences were visible in the video. Flow paths were also intermittent, as seen in the thermal images where cooler pathways through

the heated region indicative of liquid flow were observed in different locations at different times.

REEs frequently occurred in the boiling regions. Pressure pulses from the REEs were detected at substantial distances from the REEs, even though a presumed low-flow-resistance pathway (to the outlet) was present near the REEs. Extending these results to the potential nuclear-waste repository at Yucca Mountain, in a heated drift at early time, the boiling region would be nearest the drift. REEs occurring here might disturb capillary barriers (which have been assumed in many numerical modeling studies) and might even cause an intermittent spray of mineral laden water into the drift. Additionally, REEs might redistribute precipitates, which might further alter flow pathways.

2.4.3 Comparison of Current and Previous Experiments

Observations made for the current experiments support many of the observations and conclusions made for the previous x-ray radiography experiments. For instance, in one of the early experiments, a highly attenuating band was observed above the heated region. The tentative conclusion was that this could be a region of either enhanced saturation or crystal formation. Both current experiments, Experiment 1 and Experiment 2, support this conclusion. In the most recent experiments we have visual information (and x-ray images) that indicates both salt deposition and a condensation halo above the boiling region. Both mechanisms will increase x-ray attenuation through the affected areas and can impede fracture flow. Experiments FR5 and FR6 both showed the development of a thin, highly attenuating neck in or near the boiling region (Figure 7 and Figure 8). We observe similar features in the tuff/glass fracture experiments (Figure 18). Another interesting feature from experiment FR5 is the low attenuation area immediately above the highly attenuating tip (Figure 7b). This may be the region above which the condensation halo occurs. This hypothesis is supported by the presence of a highly attenuating region that includes matrix imbibition above this low attenuation zone. These features occur most prominently in the lowest flow rate/lowest hydraulic head experiments and seem to be consistent between series of experiments.

We also observe the "sponge" effect that large clasts of higher porosity have on flow and imbibition. During experiment FR5, for example, flow down the fracture stopped at a large, high-porosity clast intersected by the fracture (Figure 11a). This is similar to the change in flow properties observed during Experiment 1, where flow on the bottom right of the sample was slowed and diverted by the large clast there (Figure 10).

One further conclusion that can be made is that the processes and physical phenomena observed in the tuff tensile fractures also occur in the tuff saw cut/glass plate fracture. Thus the introduction of the smooth, non-porous glass surface does not appear to limit our ability to observe phenomena relevant to repository issues.

2.5 Conclusions

We are able to visualize phenomena related to fracture flow and matrix imbibition during fracture flow experiments at a variety of conditions and to calculate saturation within the matrix. Results indicate that under some conditions it is difficult for water to penetrate the region where temperatures are above boiling, but that water can penetrate this region under certain circumstances—for example, sufficient hydraulic head, sufficient flow rate, or in a fracture aperture. Additional experiments where head was increased indicate penetration of the boiling region. Fracture flow stopped or slowed significantly when a region of porosity

higher than the surrounding matrix was encountered. Heating a nearly saturated rock/fracture sample drove water out of the fracture on a very short time scale. These results provide important input needed for understanding coupled thermal-hydrologic-chemical processes and models of repository-design-based performance.

Rapid evaporation events (REEs) are frequently observed, and pressure pulses from these events have been observed in glass fracture models and in a hanging column of water at an appreciable distance compared to the physical size of the REEs. The magnitude of the pressure pulses generated by the REEs has not been quantified. REEs likely begin at a constricted nucleation site where bubble nucleation begins but is hindered by capillary pressure induced by the geometry of the site. In order for boiling to occur, the temperature must increase above the normal boiling point, until the nucleation is able to proceed in spite of the hindrance and the superheated liquid rapidly evaporates. REEs observed in glass fracture models have ranged in size from very small to large enough to send a visible vapor cloud several centimeters. The pressure pulses generated by REEs may affect capillary barriers and may alter thermal conditions at the potential nuclear waste repository at Yucca Mountain.

A comparison of experiments performed on tuff/glass plate fractures and tuff tensile fractures indicates that similar phenomena are observed. Thus the addition of the glass plate permits the collection of both visual and thermal information. Directions for future work include the assessment of back-fill, drip shield, and capillary barrier models by construction of essentially two-dimensional models similar in aspect ratio to the sample shown in Figure 5. These could then be heated and analyzed for effectiveness in preventing rewetting as water is introduced to the top of the sample.

3. References

Brodsky, N.S., Riggins, M., Connolly, J., and Ricci, R. 1996. *Thermal Expansion, Thermal Conductivity, and Heat Capacity Measurements for Boreholes UE25 NRG-4, UE25 NRG-5, USW NRG-6, and USW NRG-7/7A.* SAND95-1955. Albuquerque, New Mexico: Sandia National Laboratories. MOL.19970723.0031.

Buscheck, T.A., and Nitao, J.J. 1992. "The Impact of Thermal Loading on Repository Performance at Yucca Mountain." *Proceedings of the Third International Conference on High-Level Radioactive Waste Management.* pp. 1003-1017. La Grange Park, Illinois: American Nuclear Society. NNA.19920408.0008. (Also UCRL-JC-109232, Lawrence Livermore National Laboratory, Livermore, California)

Cary, J.W., and Taylor, S.A. 1962. "The interaction of the simultaneous diffusions of heat and water." *Soil Sci. Soc. Am. J.* **26**:413–420.

Cass, A., Campbell, G.S., and Jones, T.L. 1984. "Enhancement of thermal vapor diffusion in soil." *Soil Sci. Soc. Am. J.* **48**(1):25–32.

Chung, P.K., and Jackson, M.L. 1954. "Thermal diffusivity of low conductivity materials." *Ind. Eng. Chem.* **46**:2563–2566.

Hopmans, J.W., and Dane, J.H. 1986. "Thermal conductivity of two porous media as a function of water content, temperature and density." *Soil Sci.* **142**:187–195.

Lide, D.R. 1990. *Handbook of Chemistry and Physics.* (71st edition) Boca Raton, Florida: CRC Press, Inc.

Nitao, J.J., and Buscheck, T.A. 1991. "Infiltration of a liquid front in an unsaturated, fractured porous medium." *Water Resources Res.* **27**(8):2099–2112. NNA.19920131.0319. (Also UCRL-JC-107092, Lawrence Livermore National Laboratory, Livermore, California)

Parikh, R.J., Havens, J.A., and Scott, H.D. 1979. "Thermal diffusivity and conductivity of moist porous media." *Soil Sci. Soc. Am. J.* **43**:1050–1052.

Philip, J.R., and DeVries, D.A. 1957. "Moisture movement in porous materials under temperature gradients." *Trans. Am. Geophys. Union* **38**(2):222–232. NNA.19890713.0173.

Phillips, O.M. 1994. "Liquid Infiltration through the Boiling-Point Isotherm in a Desiccating Fractured Rock Matrix." *Proceedings of the Fifth International Conference on High-Level Radioactive Waste Management.* La Grange Park, Illinois: American Nuclear Society.

Phillips, O.M. 1996. "Infiltration of a liquid finger down a fracture into superheated rock." *Water Resources Res.* **32**:1665–1670.

PMIC 1998. *Specific Heat Measurements of Rock Material.* July 21, 1998. Philomath, Oregon: Precision Measurements and Instruments Corp. DTN LL980916204242.056.

Roberts, J.J., and Lin, W. 1996. "X-ray Radiography of Fracture Flow and Matrix Imbibition." *Proceedings of the Seventh International Conference on High-Level Radioactive Waste Management.* pp. 89-91. La Grange Park, Illinois: American Nuclear Society. MOL.19960408.0177. (Also UCRL-JC-122504, Lawrence Livermore National Laboratory, Livermore, California)

Roberts, J.J., and Lin, W. 1997. "X-Ray radiography of fracture flow and matrix imbibition in Topopah Spring tuff under a thermal gradient." *Int. J. Rock Mech. Min. Sci.* 34(3–4). MOL.19980105.0514. (Paper no. 259; also UCRL-JC-125612, Lawrence Livermore National Laboratory, Livermore, California)

Wilder, D.G. 1996. *Near-Field and Altered-Zone Environment Report, Volume II.* UCRL-LR-124998, Vol. II. Livermore, California: Lawrence Livermore National Laboratory. MOL.19961212.0121. MOL.19961212.0122.

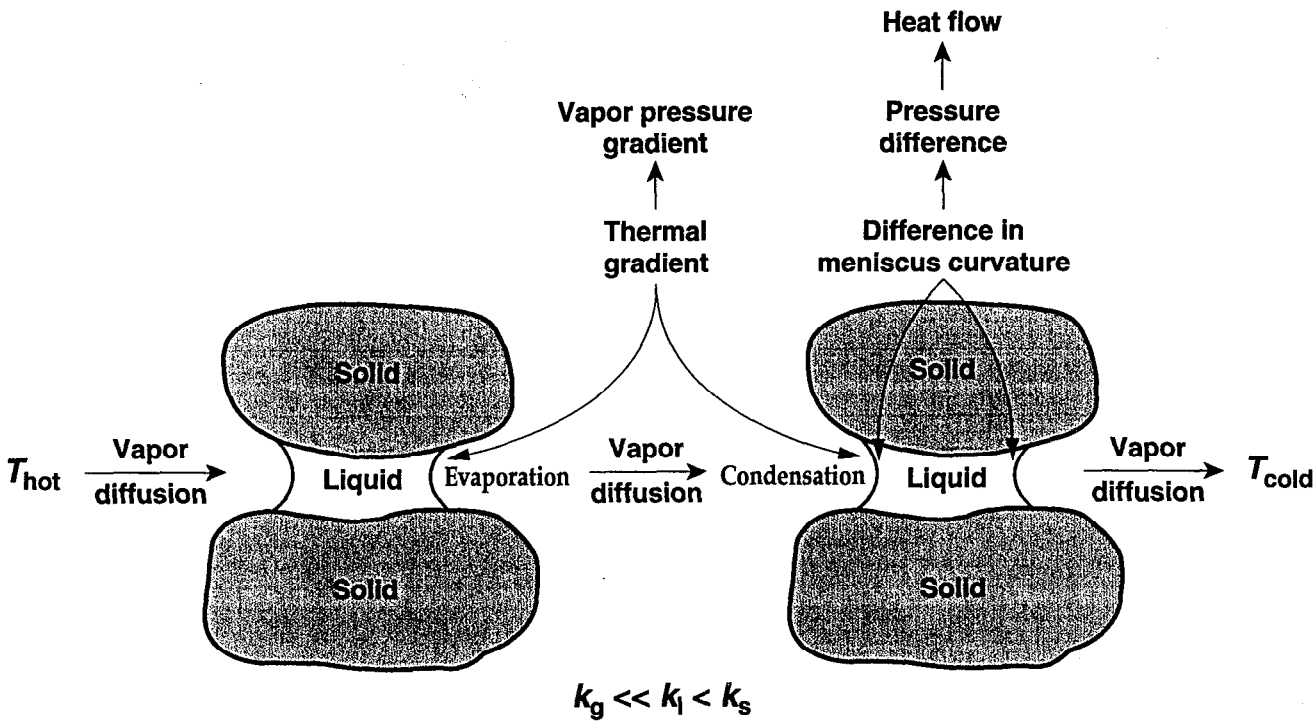

Figure 1. Liquid film between two soil grains forming a barrier to vapor transport

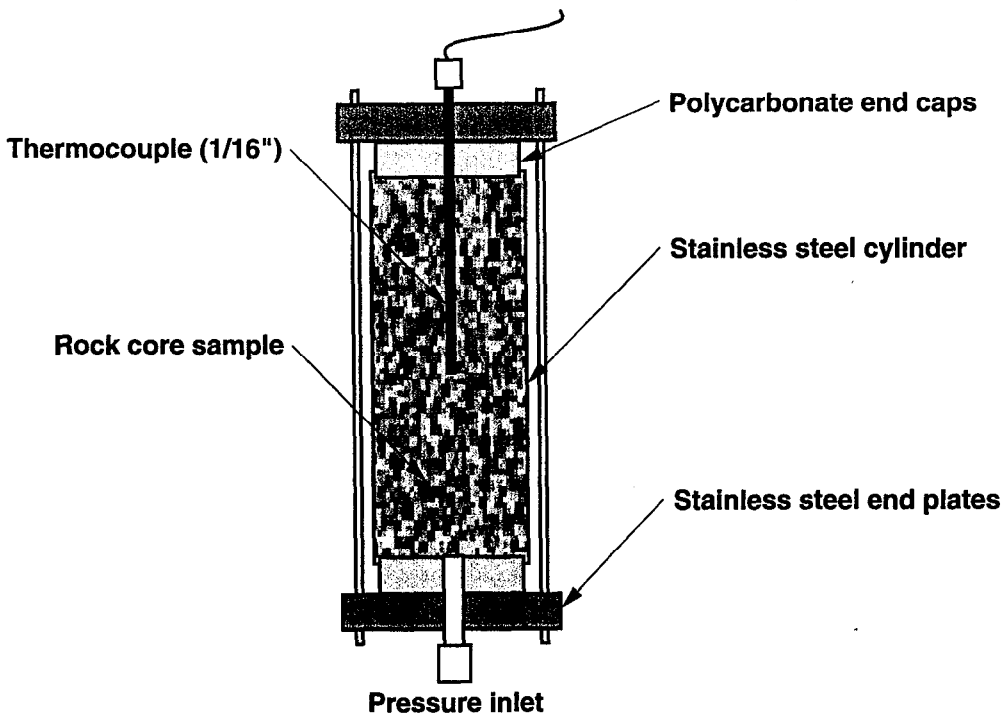

Figure 2. Schematic of the pressure cell holding the rock core

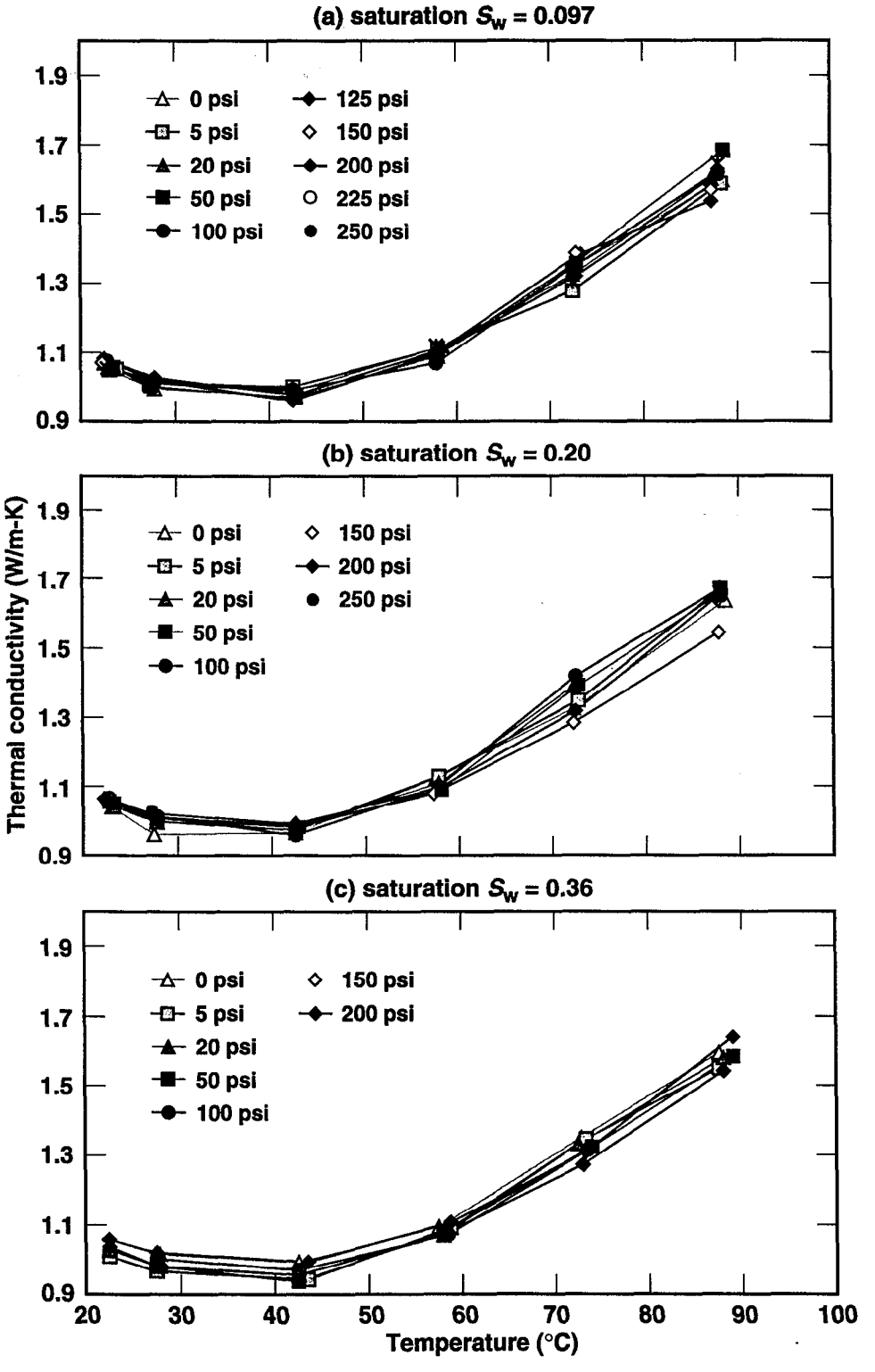

Figure 3. Thermal conductivity of Topopah Spring tuff as a function of temperature and pressure (DTN LL980913104242.051). (a) for saturation S_w = 0.097 (water content θ = 0.008 cm^3/cm^3) (b) for saturation S_w = 0.20 (water content θ = 0.017 cm^3/cm^3) and (c) for saturation S_w = 0.36 (water content θ = 0.030 cm^3/cm^3)

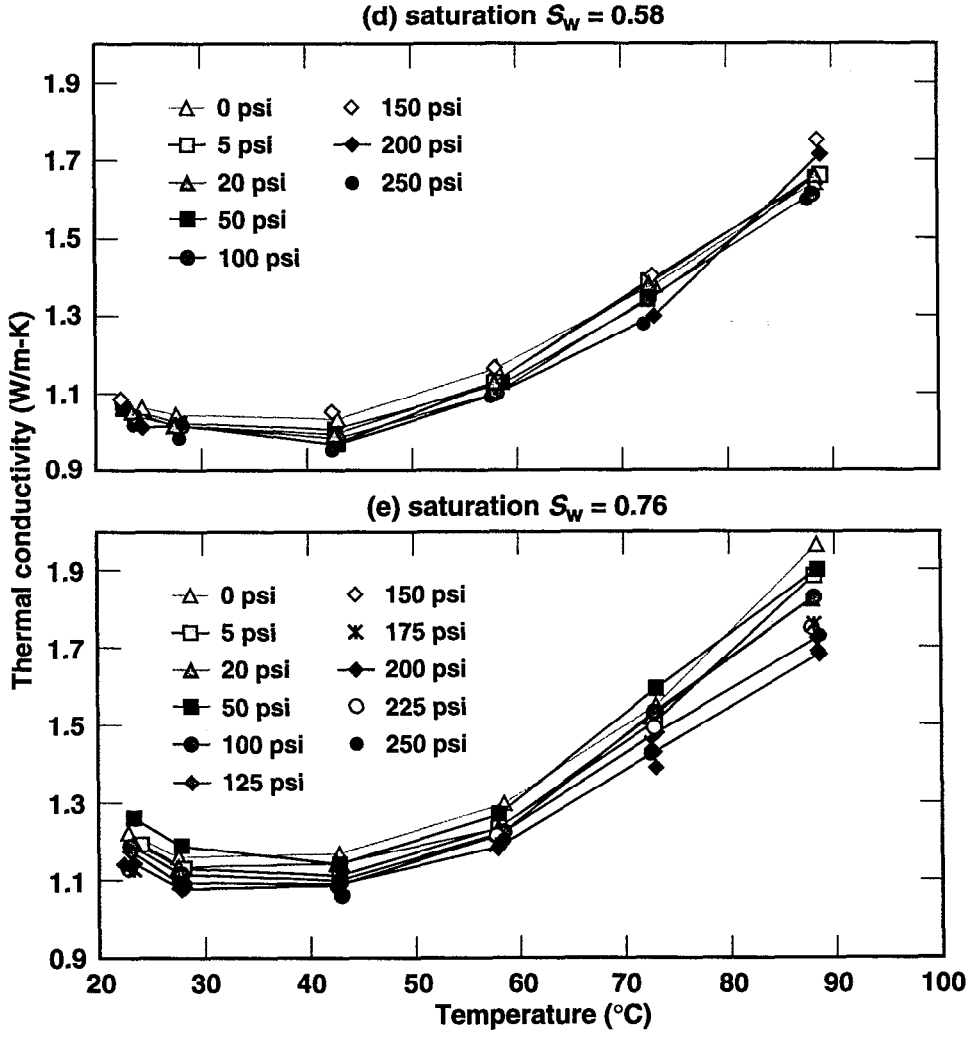

Figure 3 (continued). Thermal conductivity of Topopah Spring tuff as a function of temperature and pressure (DTN LL980913104242.051). (d) for saturation $S_w = 0.58$ (water content $\theta = 0.048$ cm^3/cm^3) and (e) for saturation $S_w = 0.76$ (water content $\theta = 0.062$ cm^3/cm^3)

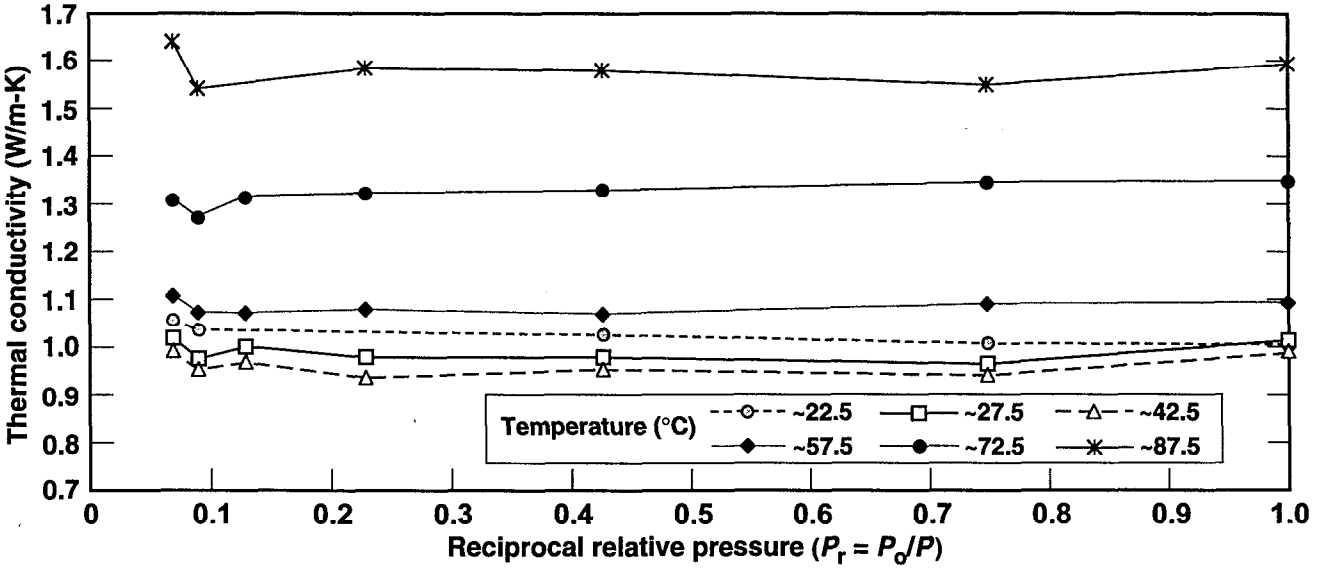

Figure 4. Thermal conductivity of Topopah Spring tuff as a function of temperature and reciprocal relative pressure for $S_w = 0.36$ ($\theta = 0.030$ cm^3/cm^3) (DTN LL980913104242.051)

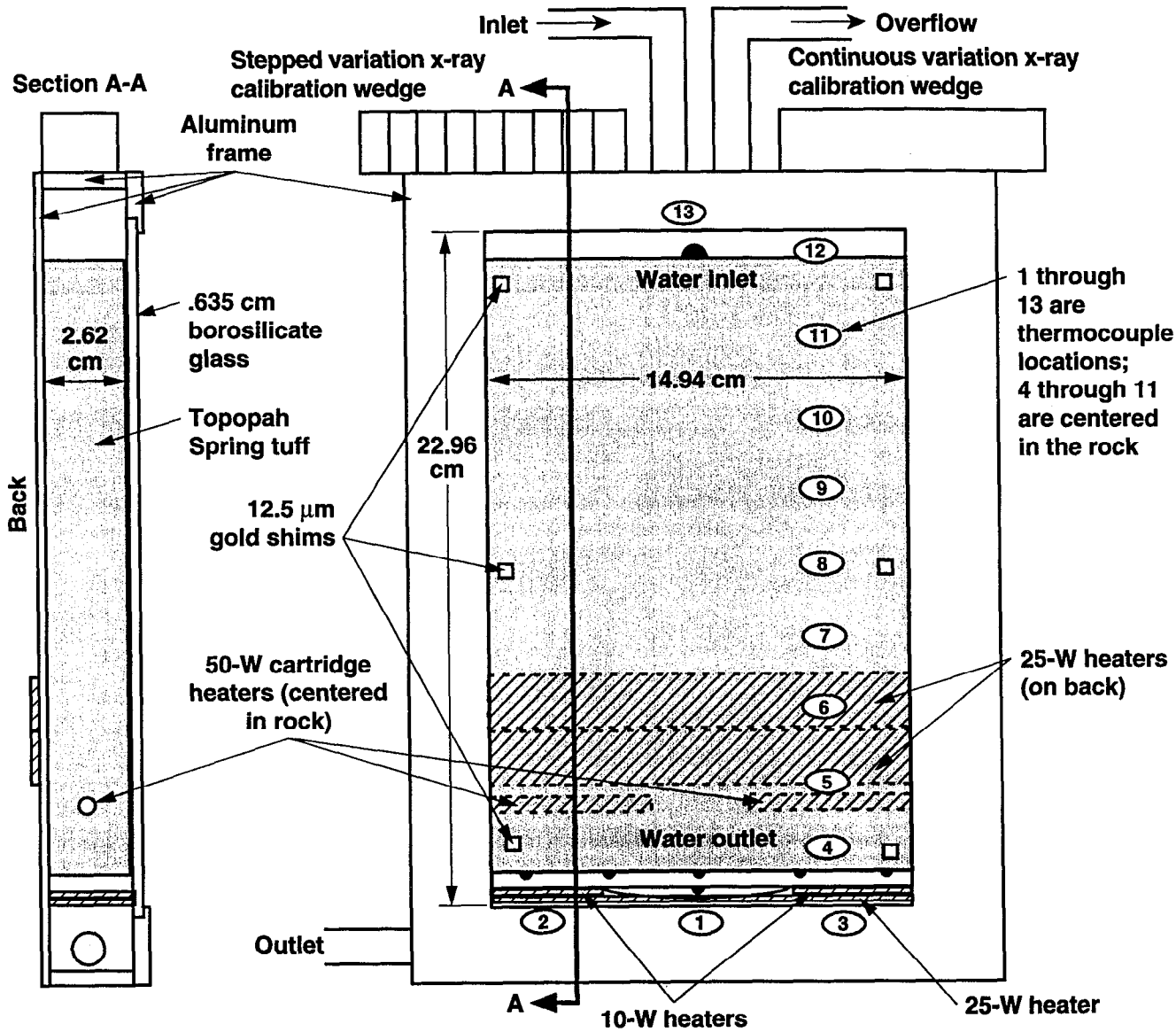

Figure 5. Experimental apparatus

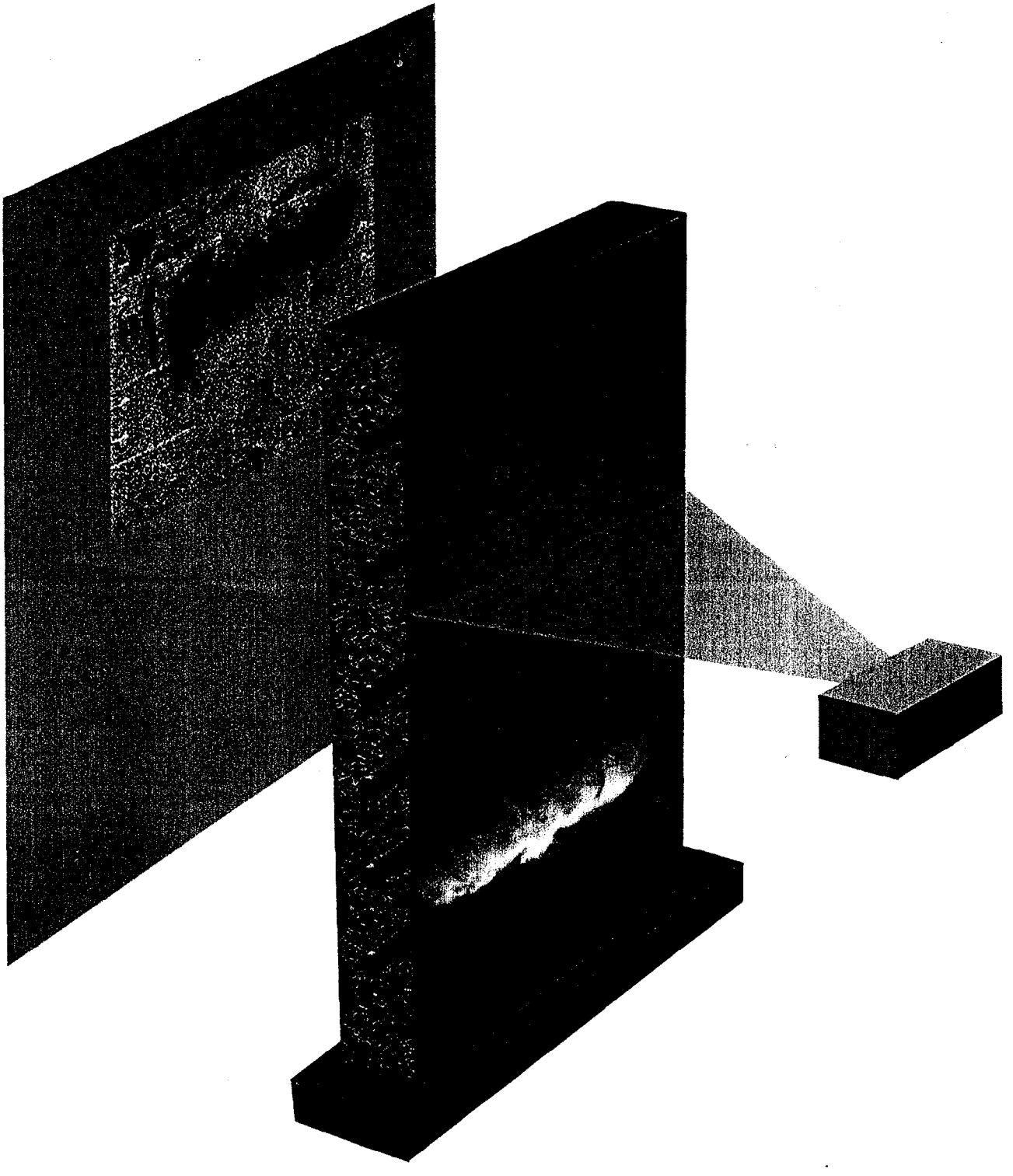

Figure 6. Schematic of x-ray radiograph system. Sample translates vertically through the 160-kVp linear source. Detector stores digital data, line by line. One scan takes between one and two minutes, depending on sample height. Thermal and video imaging were concurrent.

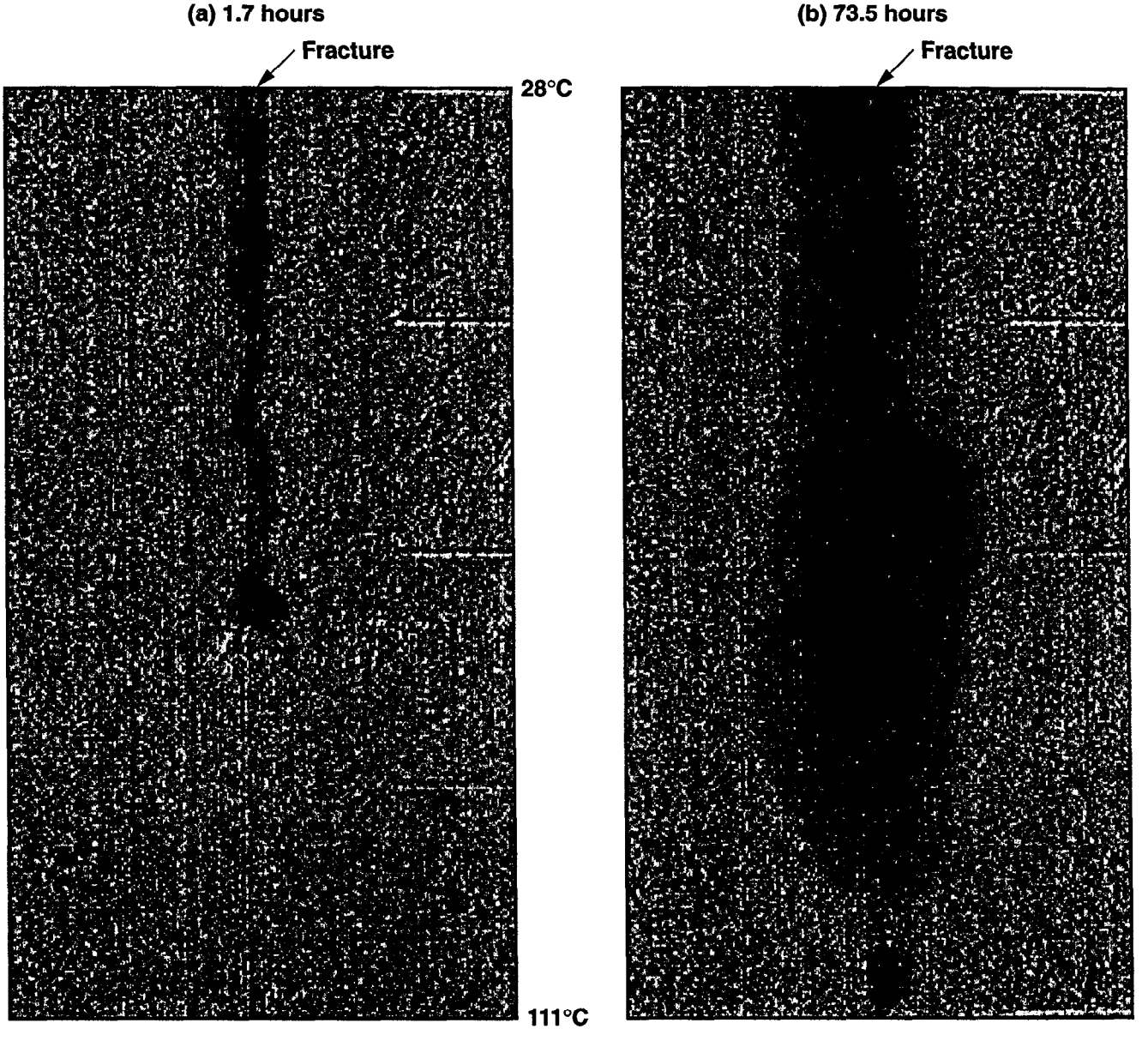

Figure 7. Difference radiographs of FR5. Darker shades indicate increased x-ray attenuation compared to the initial image, and hence, increased saturation. Images were taken 1.7 (a) and 73.5 (b) hours after flow was initiated. The first image shows a stoppage of flow along the fracture caused by the presence of a relatively porous region intersected by the fracture. The second image shows progression of the wetting front past the highly porous region to the boiling zone.

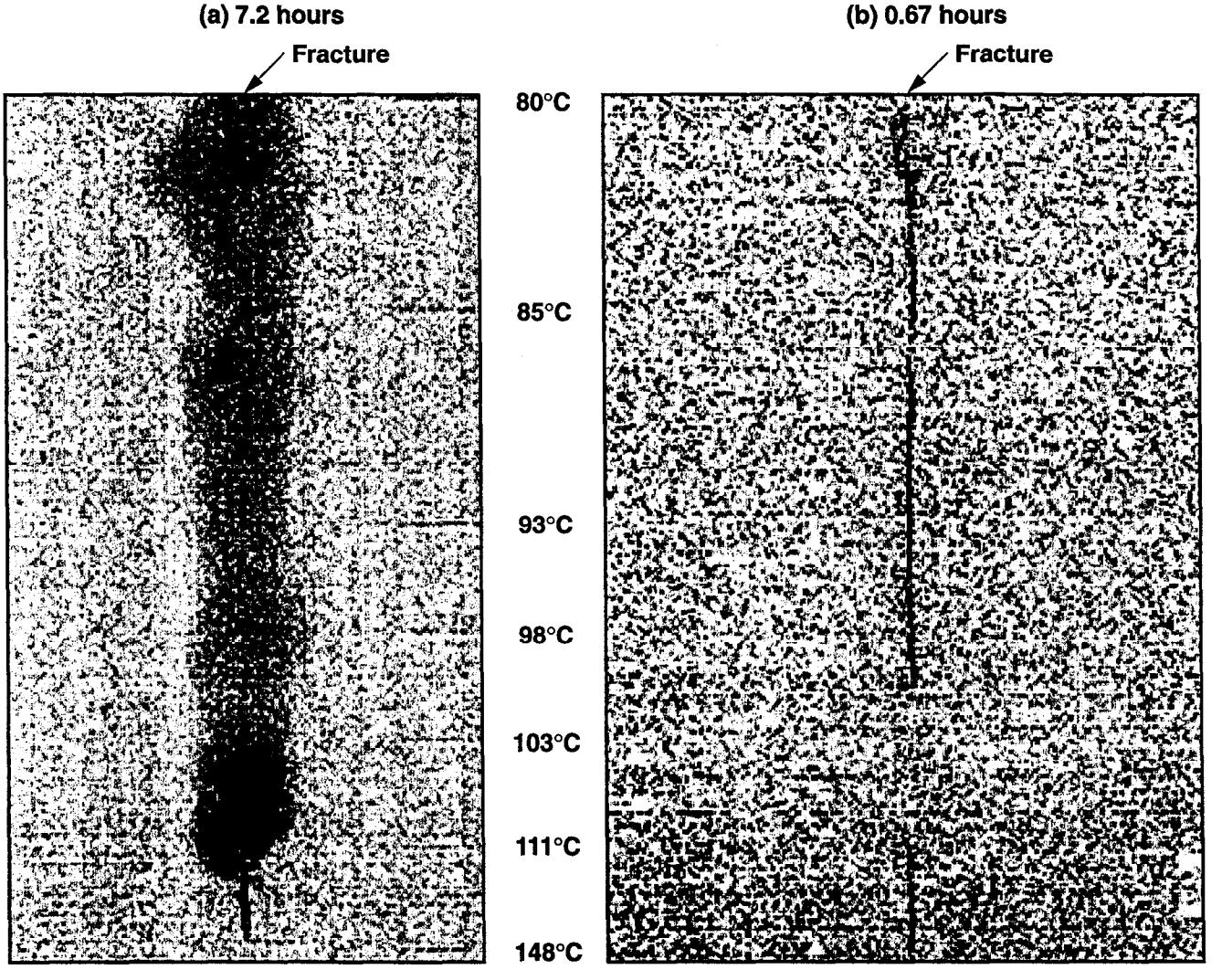

Figure 8. Difference images of FR6 (a) and FR6b (b), 7.2 and 0.67 hours after flow was initiated. Thermal gradient is indicated between the figures. The difference between these two experiments was the height of the water column, 0.26 and 0.46 m, for FR6 and FR6b respectively. The difference in head was large enough to force flow through the boiling region during FR6b.

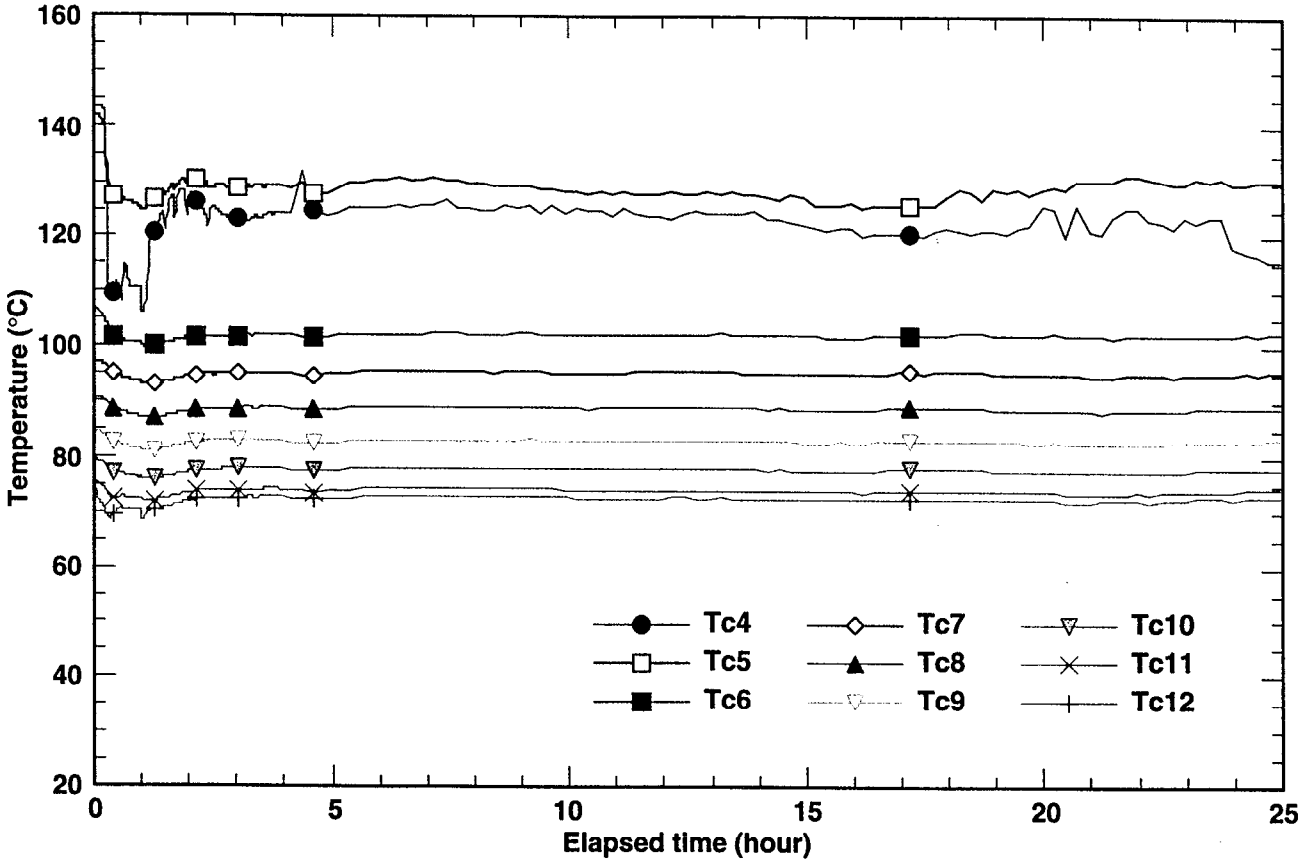

Figure 9. Temperature history of Thermocouples 4 through 12, Experiment 1

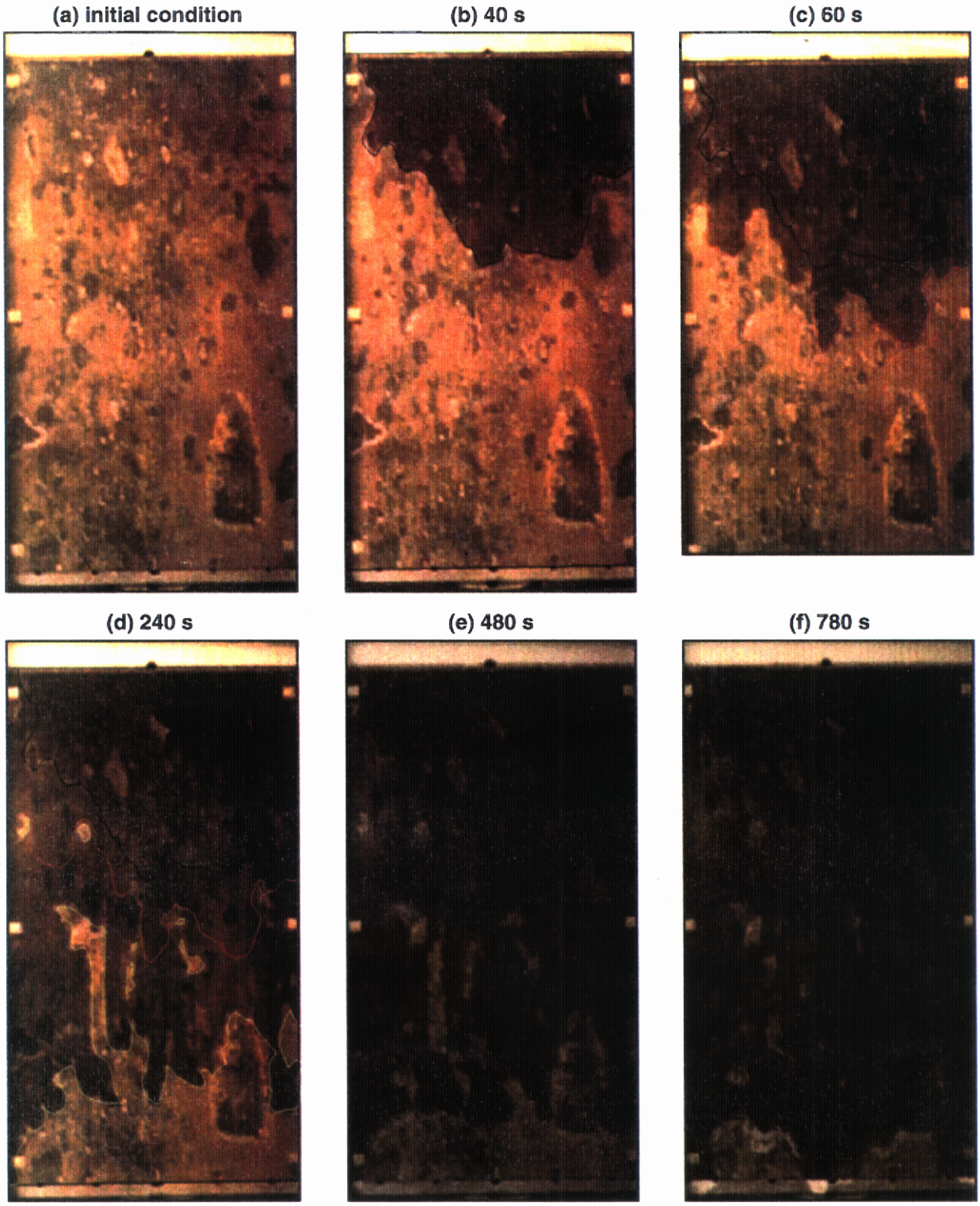

Figure 10. Video images of initial condition and seepage in tuff/glass fracture, Experiment 1

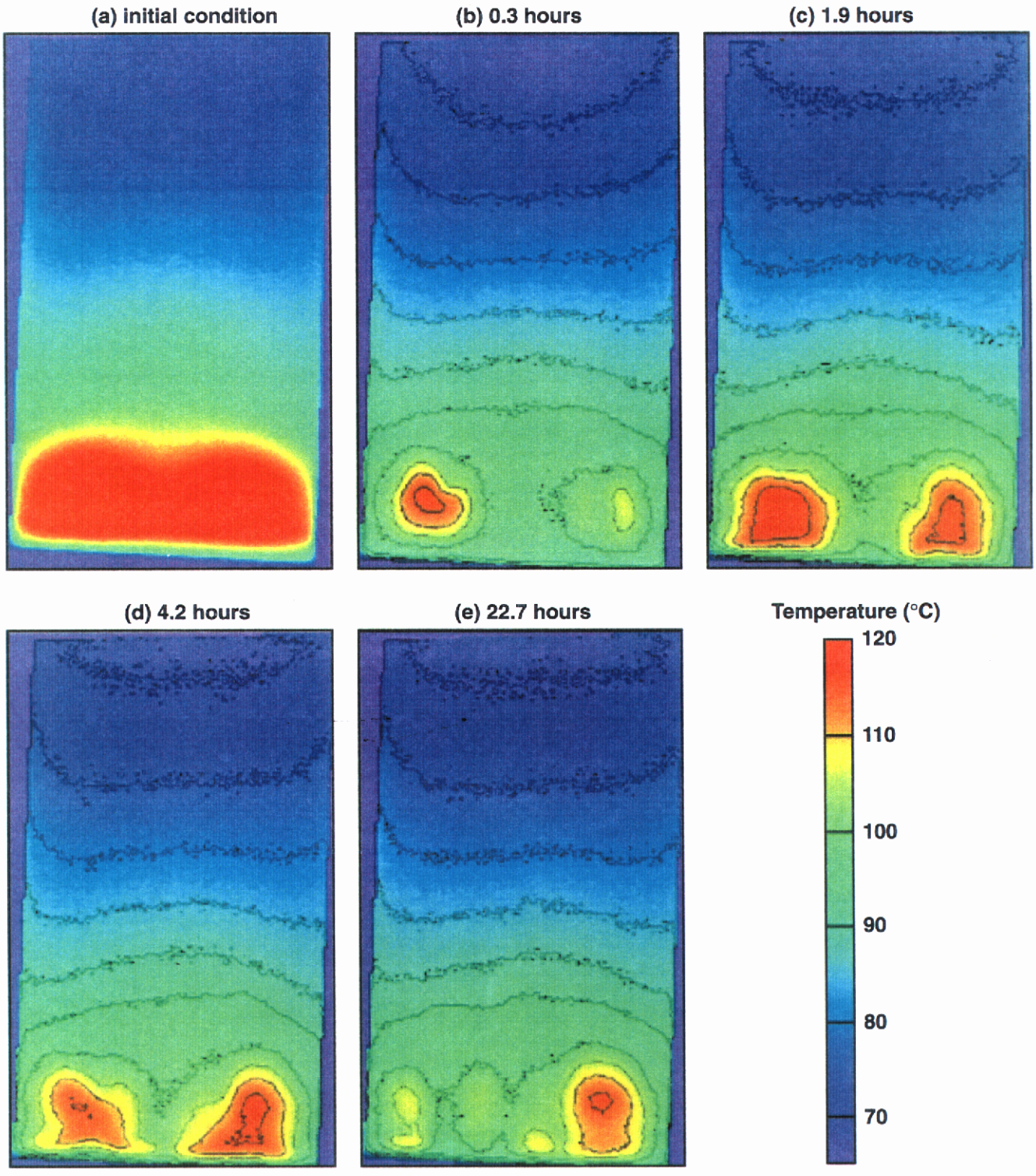

Figure 11. Initial and subsequent temperature distributions of the outer glass surface, Experiment 1

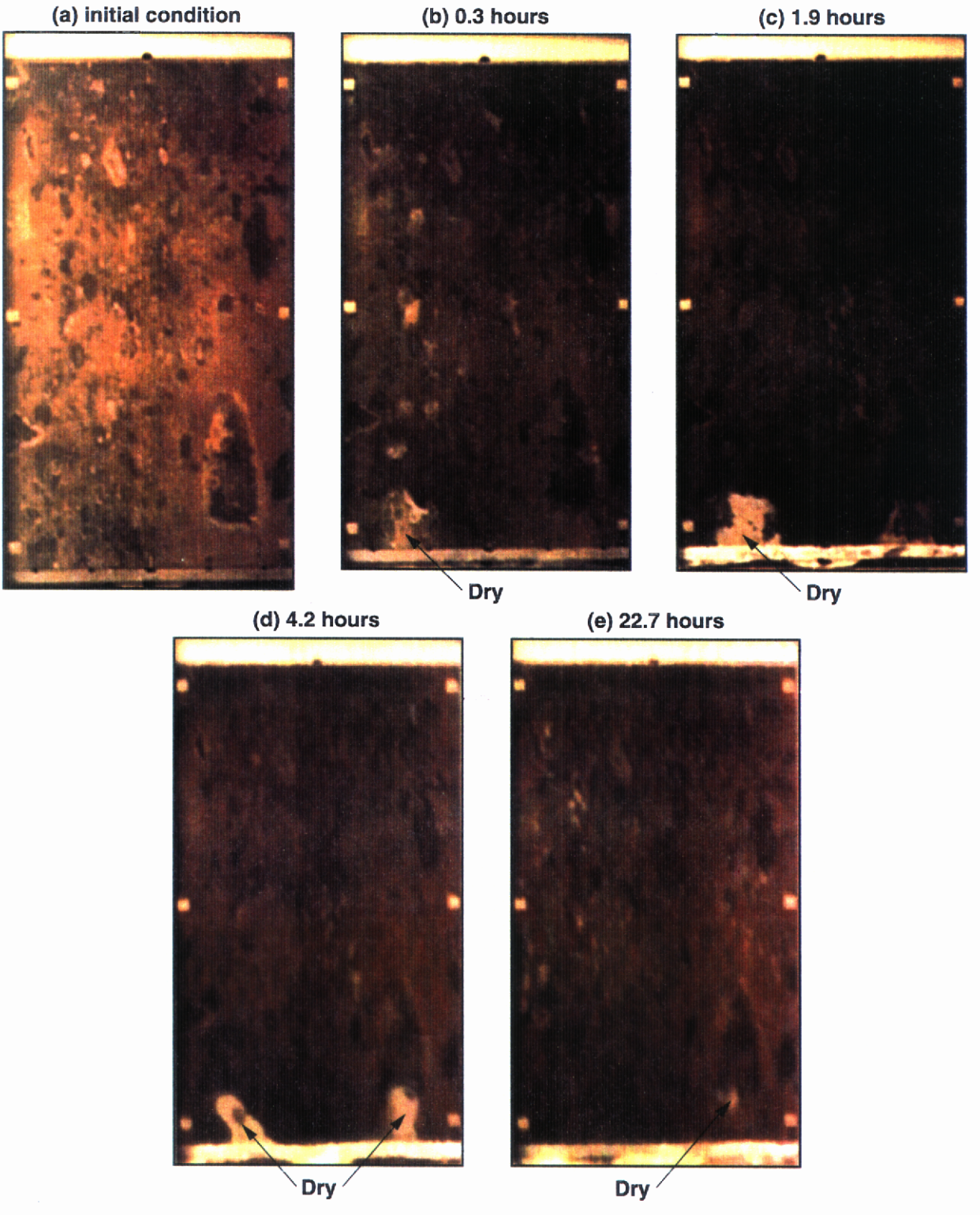

Figure 12. Video images taken at the indicated times, Experiment 1

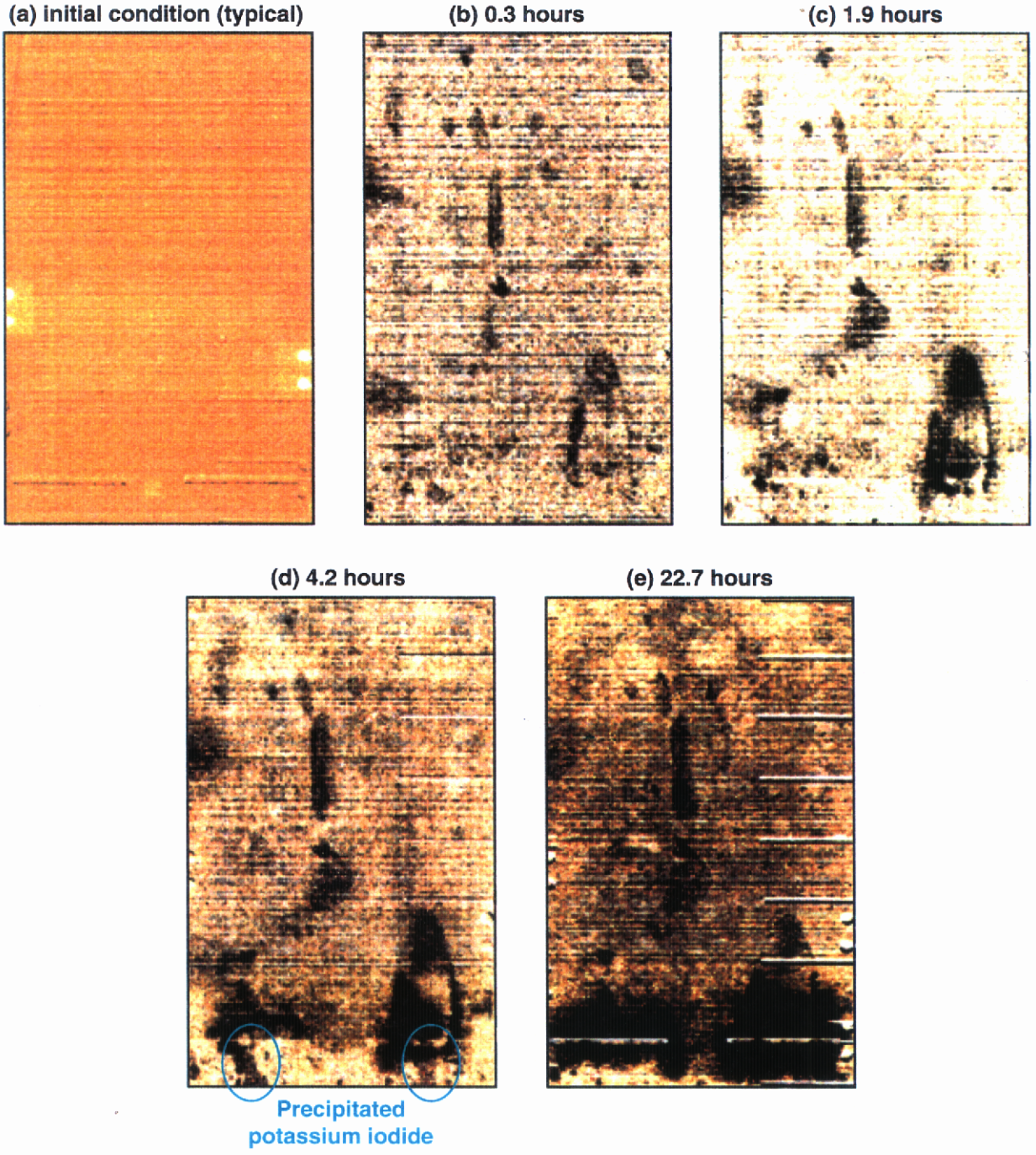

Figure 13. X-ray attenuation difference images indicating imbibition and potassium iodide precipitation over time, Experiment 1. Darker shades indicate more attenuation, thus more imbibition or crystal precipitation. In (d), circled areas are visible as precipitated potassium iodide in Figure 10.

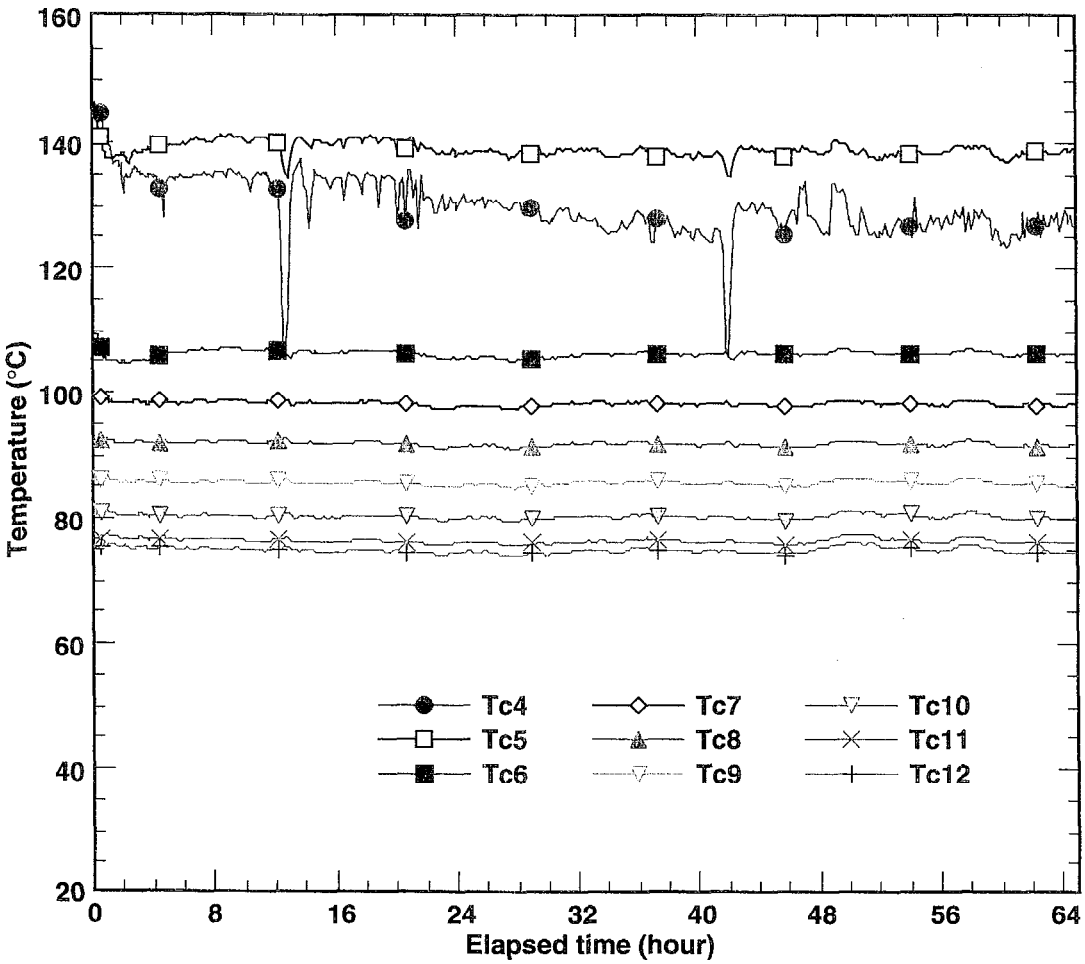

Figure 14. Temperature history for thermocouples 4 through 12 for Experiment 2.

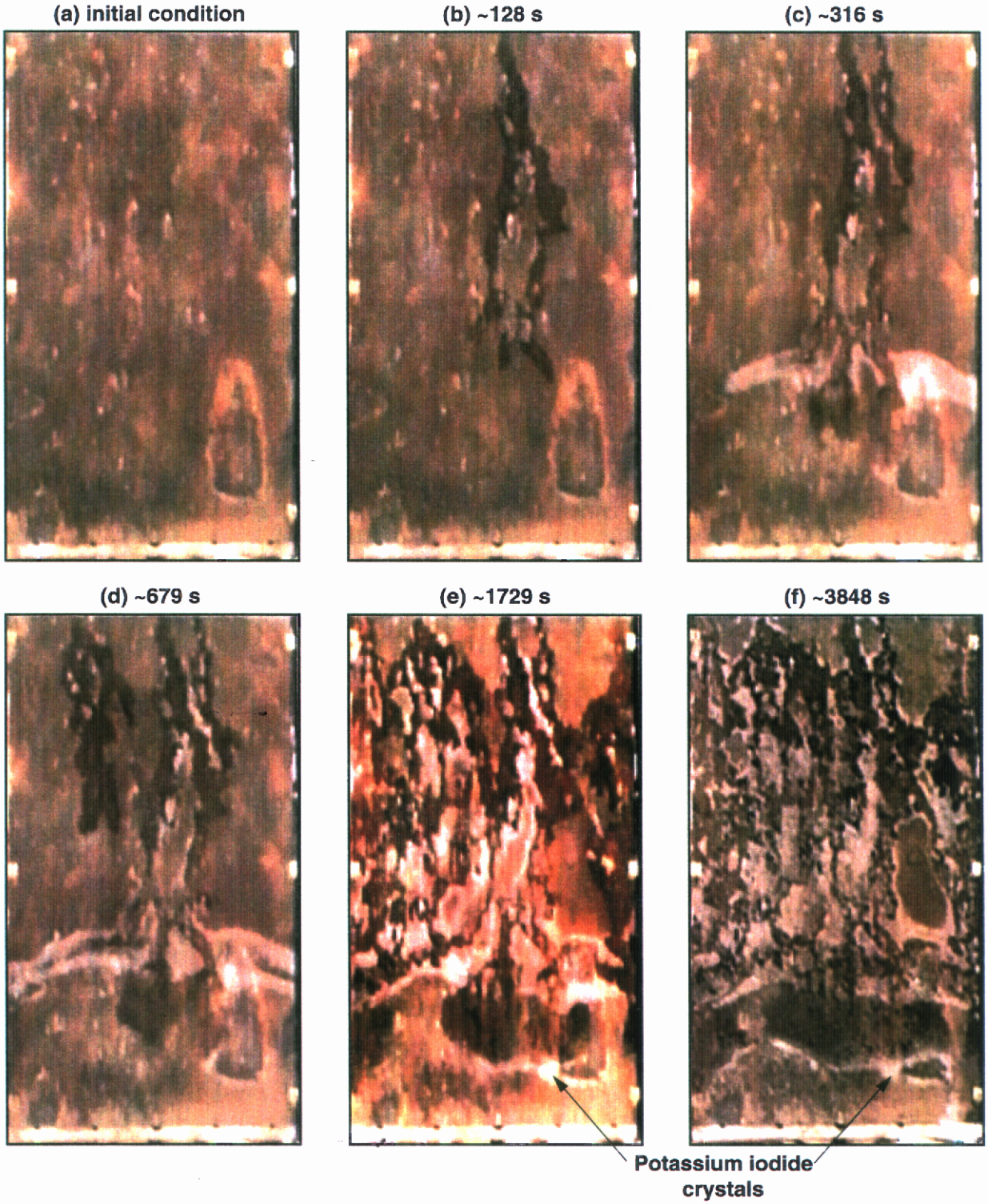

Figure 15. Video image of initial condition, seepage, and condensation halo formation, Experiment 2 Arrow points to potassium iodide crystals.

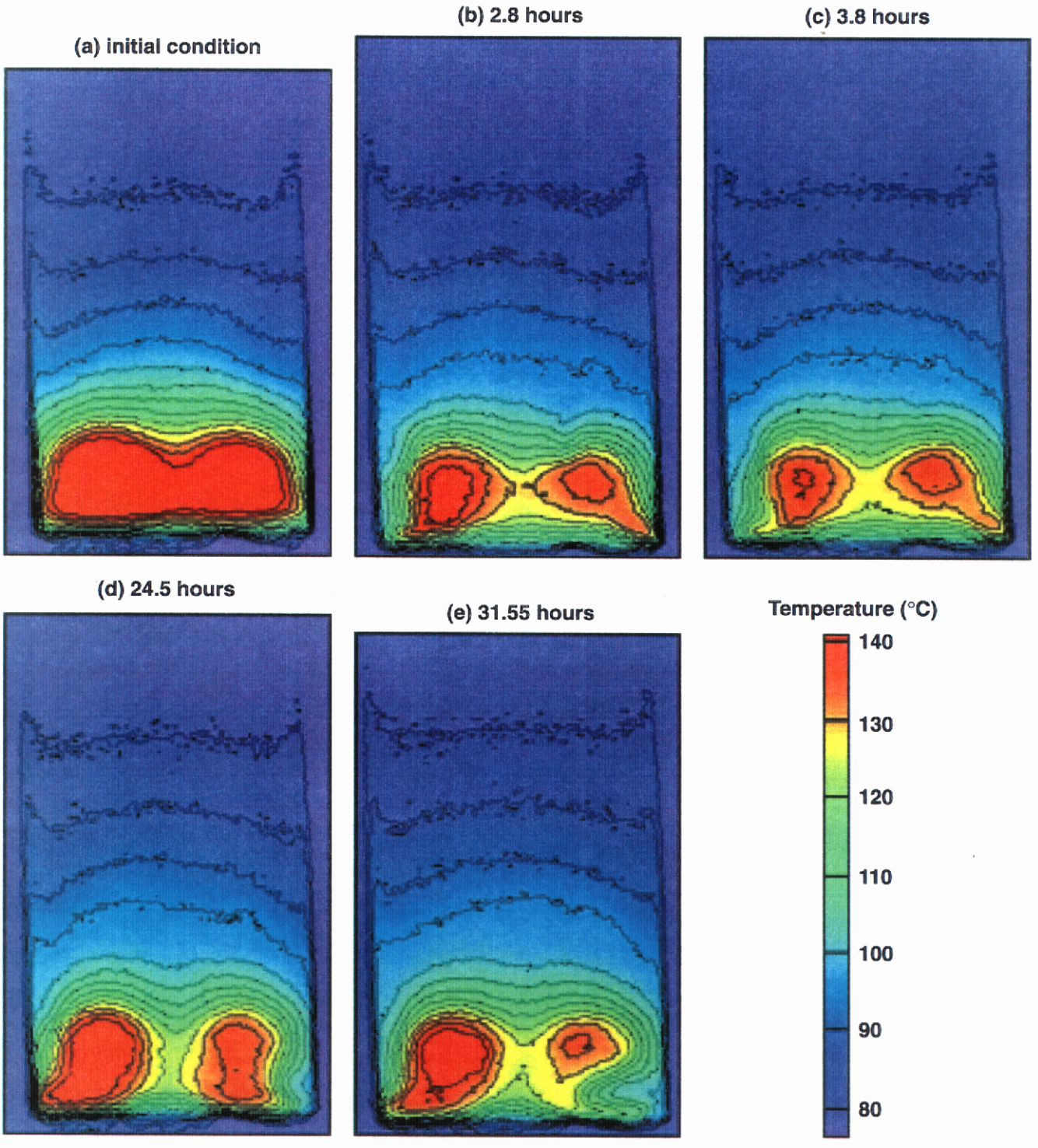

Figure 16. Initial and subsequent temperature distributions of the outer glass surface, Experiment 2

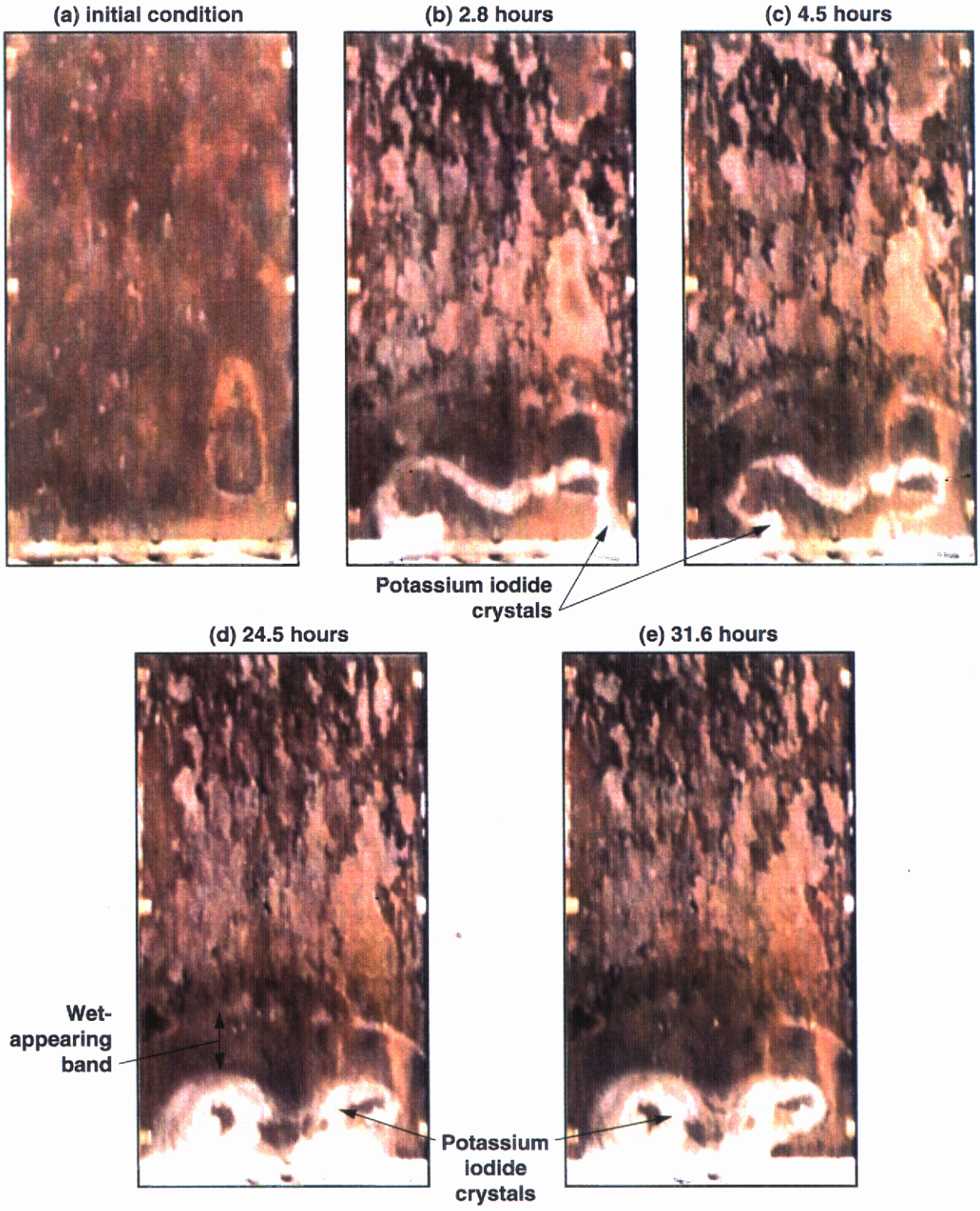

Figure 17. Video images taken at the indicated times, Experiment 2. The wet-appearing band is indicated in (d). Arrows point to potassium iodide crystals.

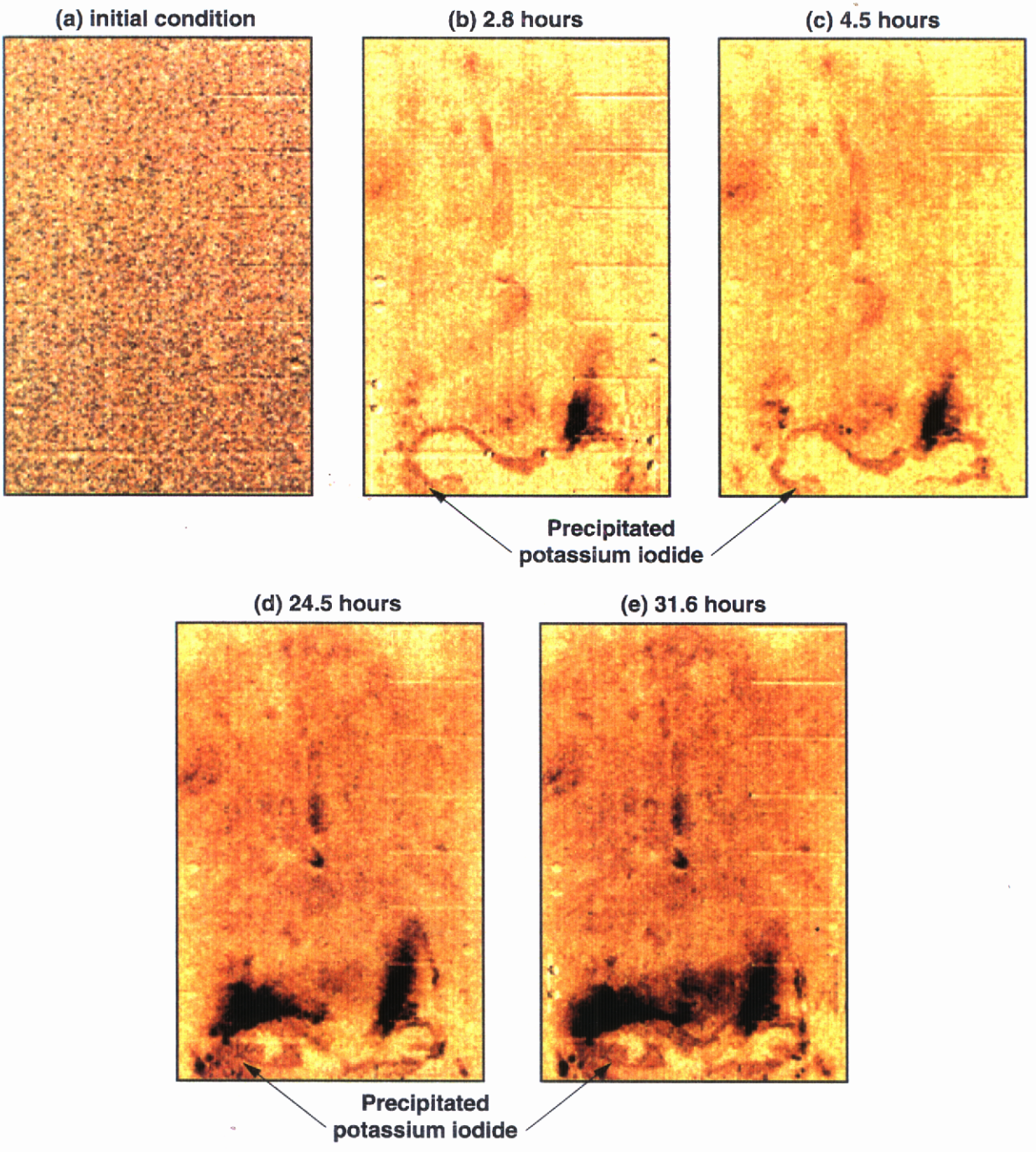

Figure 18. X-ray attenuation difference images indicating imbibition and potassium iodide precipitation over time, Experiment 2. Darker shades indicate more attenuation, thus more imbibition or precipitation. Indicated areas are visible as precipitated potassium iodide in Figure 15.